



Contents lists available at ScienceDirect

International Journal of Solids and Structures

journal homepage: www.elsevier.com/locate/ijsolstr

Electrically-tunable active metamaterials for damped elastic wave propagation control

Giacomo Elefante^a, Maria Laura De Bellis^{b,*}, Andrea Bacigalupo^c^a University of Padova, Department DM, Via Trieste 63, Padova, Italy^b University of Chieti-Pescara, Department INGEO, Viale Pindaro 42, Pescara, Italy^c University of Genoa, Department DICCA, Via Montallegro 1, Genoa, Italy

ARTICLE INFO

Keywords:

Tunable metamaterials
Active control
Dissipative shunted circuits

ABSTRACT

An electrically-tunable metamaterial is herein designed for the active control of damped elastic waves. The periodic device is conceived including both elastic phases and a piezoelectric phase, shunted by a dissipative electric circuit whose impedance/admittance can be adjusted on demand. As a consequence, the frequency band structure of the metamaterial can be modified to meet design requirements, possibly changing over time. A significant issue is that in the presence of a dissipative circuit, the frequency spectra are obtained by solving eigen-problems with rational terms. This circumstance makes the problem particularly difficult to treat, either resorting to analytical or numerical techniques. In this context, a new derationalization strategy is proposed to overcome some limitations of standard approaches. The starting point is an infinite-dimensional rational eigen-problem, obtained by expanding in their Fourier series the periodic terms involved in the governing dynamic equations. A special derationalization is then applied to the truncated eigen-problem. The key idea is exploiting a LU factorization of the matrix collecting the rational terms. The method allows to considerably reduce the size of the problem to solve with respect to available techniques in literature. This strategy is successfully applied to the case of a three-phase metamaterial shunted by a series RLC circuit with rational admittance.

1. Introduction

Metamaterials are engineered structured materials, typically incorporating sub-wavelength arrays of resonant unit cells, specially designed to achieve exotic properties well beyond what is possible with conventional materials. Applications, including sound filtering (Cummer et al., 2016; Iannace et al., 2021; Xiang et al., 2022), antennas (Tadesse et al., 2020; Kumar et al., 2021), seismic protection (Brûlé et al., 2014; Achaoui et al., 2016; Colombi et al., 2016; Carta et al., 2016; Miniaci et al., 2016; Achaoui et al., 2017), guided mode manipulation (Liao and Zhao, 2020; Guo et al., 2020), energy harvesting (De Bellis et al., 2019; Alshaqqa and Erturk, 2020; De Ponti et al., 2020; Hu et al., 2021), as well as cloaking devices (Brun et al., 2009; Norris and Shuvalov, 2011; Stenger et al., 2012; Colquitt et al., 2014; Misseroni et al., 2016; Zhang et al., 2020) and superlenses (Yan et al., 2013; Park et al., 2015; Brun et al., 2019), span from optics to elastodynamics and acoustics. With reference to the last two mentioned areas of interest, the key concept to achieving smart mechanical properties is to appropriately design the microstructure (shape, geometry, size, orientation and arrangement) of metamaterials also possibly including active

phases. The resulting microstructured materials are capable of showing fascinating behaviours such as ultra-stiffness/super-strength (Al-Ketan et al., 2018; Momeni et al., 2019; Zhang et al., 2022), high fracture toughness (Jia and Wang, 2019; Yin et al., 2021), ultra-lightness (Wang et al., 2021; Chen et al., 2022; Zhang and Xu, 2022), auxeticity (Bacigalupo and Gambarotta, 2016; Cabras and Brun, 2016; Lu et al., 2017; Willey et al., 2020; Diana et al., 2023), as well as extreme constitutive behaviours (Barchiesi et al., 2019; Zangeneh-Nejad and Fleury, 2019; Bhatt and Banerjee, 2022) and wave manipulation properties (Bacigalupo and Gambarotta, 2017; Beli et al., 2018; Bordiga et al., 2021, 2022; Ghaffarivardavagh et al., 2018; Mu et al., 2020). The rising attention, shown in last years in this field, testifies to the growing interest to pushing the existing limits of the mechanics of materials in order to design increasingly versatile and efficient metadevices. In this regard, the potential of 3D printing can often be exploited to advantage (Yuan et al., 2019; Sangiorgio et al., 2022; Montgomery et al., 2020; Gavazzoni et al., 2022).

In this context, an intriguing idea, which can be favourably leveraged in the design of high-performance metamaterials properly conceived for the wave propagation control, is the use of active phases

* Corresponding author.

E-mail address: marialaura.debellis@unich.it (M.L. De Bellis).<https://doi.org/10.1016/j.ijsolstr.2023.112306>

Received 13 January 2023; Received in revised form 24 April 2023; Accepted 3 May 2023

Available online 11 May 2023

0020-7683/© 2023 The Authors. Published by Elsevier Ltd. This is an open access article under the CC BY license (<http://creativecommons.org/licenses/by/4.0/>).

responsible for multi-field couplings, such as the electro-, thermo-, chemo- or the magneto-mechanical one (Xiao et al., 2020). In other terms, by harnessing field responsive materials in the design of the microstructure, a broad range of mechanical responses are possible without changing the mass of the system. Among others, the electro-mechanical coupling provided by piezoelectric materials has been successfully exploited and gave rise to many applications comprehensively listed in review papers (Chen et al., 2018; Marakakis et al., 2019; Zangeneh-Nejad and Fleury, 2019). A first contribution in this area dates back to the end of the seventies with the seminal work by Forward (Forward, 1979) demonstrating the effectiveness of using external electronic circuits to damp mechanical vibrations in optical systems. The basic principle is the use of piezoelectric elements shunted by electrical networks (shunted piezoelectric phases), resorting to either active or passive control schemes. In the latter case, the piezoelectric phases are shunted to passive electrical circuits (Hagood and von Flotow, 1991; Hollkamp, 1994; Preumont, 1997; Thomas et al., 2009). From a technological point of view, shunting can be achieved either by applying patches of piezoelectric material on host structures (dell'Isola et al., 2004; Casadei et al., 2009; Yi and Collet, 2021; Wang et al., 2011; Zhang et al., 2015; Thorp et al., 2001; Airoidi and Ruzzene, 2011; Collet et al., 2012; Bergamini et al., 2015; Ouisse et al., 2016; Chen et al., 2017) or directly by including a shunted phase in the topology of the composite material (Flores Parra et al., 2017; Hou and Assouar, 2018; Dwivedi et al., 2020; Bacigalupo et al., 2020, 2022). Interesting studies also relate to spatially reversible and programmable piezoelectric metamaterial (Celli et al., 2017, 2018; Alan et al., 2019), as well graded piezoelectric shunted (Jian et al., 2022). On the other hand a detailed review of different active mechanical metamaterials can be found in Pishvar and Harné (2020), Ji and Huber (2022).

Focusing on the research targeted to realize tunable mechanical metamaterials, in this paper we propose a paradigm to design electrically-tunable active metamaterials for the propagation control of damped elastic waves. In Bacigalupo et al. (2020) a three phase periodic metamaterial characterized by a phononic crystal coupled to local resonators has been proposed with a phase shunted by an electrical circuit. The constitutive relations derived are valid in general, independent of the type of electrical circuit considered, whether it is dissipative or non-dissipative. Nevertheless the range of explored applications focuses on the case of a purely capacitive, non-dissipative circuit. This circumstance is because, in the presence of a dissipative circuit, the analysis of wave propagation involves rational eigen-problems which are very difficult to attack, both resorting to analytical and computational methods. To overcome these difficulties and being able to consider dissipative circuits, i.e. rational eigenvalue problems as well, a possible way out is the use of derationalization techniques. More specifically, with reference to a rational eigenvalue problem composed by a polynomial part and a rational part where the rational part is the sum of scalar rational functions multiplying certain constant matrices, a possible classical way to resolve it is considering a linearization of the rational part as described in Mehrmann and Voss (2004). The term linearization means that the derationalization can be carried out by multiplying the entire problem by the product of the scalar functions. This results in a polynomial eigenvalue problem of higher degree which can be resolved by a linearization process as the ones described in Mackey et al. (2006b,a) and their references within. This approach can only be applied to small-scaled problems. Another strategy to attack the rational eigenvalue problem is to consider it as a general nonlinear eigenvalue problem and solve it by using some nonlinear eigensolver as the ones in Ruhe (1973) or the more recent (Lietaert et al., 2022) and their references within. Regrettably, this strategy can be only exploited to find an approximate solution of the original problem and requires a reliable convergence analysis.

Based on this context, in this paper we propose a novel enhanced derationalization technique, inspired by Su and Bai (2011), that proves

to be efficient also in the case of large-scaled problems. The main idea is to linearize the eigenproblem matrix through LU factorization, so that the linearized problem becomes significantly smaller, leading to a faster computation of the eigenvalues. The proposed methodological advance allows the study of metafilters with piezoelectric phases shunted by general RLC circuit (with rational admittance) and to explore the intriguing field of wave propagation control in the presence of damped elastic waves.

The paper is organized as follows. In Section 2 the dynamic balance equations governing the in-plane behaviour of the periodic tunable metamaterial are introduced, with a emphasis on the constitutive equations specialized for either linear elastic or shunted piezoelectric phases. Section 3 is devoted to wave propagation and frequency band structure determination in the case of general dissipative circuits. Within the validity of the Floquet theory, the Fourier series expansion of the periodic terms intervening in the balance equations leads to rational infinite dimensional rational eigen-problem. In Section 4 such eigen-problem is truncated and derationalized via the newly proposed approach. Moreover, Section 5 focuses on the particularization of the enhanced derationalization technique to the case of a specific example of RLC series circuit. In Section 6 numerical experiments are presented with the aim of investigating the effects of the tuning parameters of the electrical circuit on the overall behaviour of the designed metamaterial. Finally in Section 7 final remarks are drawn together with possible future developments.

2. Governing equations of the periodic tunable metamaterial

We focus on a periodic heterogeneous metamaterial, made of different phases distinguished between elastic and a piezoelectric phase shunted by generic electrical circuits (see Fig. 1). The metamaterial is made by the in-plane regular repetition of a periodic cell \mathfrak{A} , along its periodicity vectors. It follows that the periodic metamaterial is associated with a periodic lattice defined by the discrete subgroup $\mathcal{X} := \{\mathbf{X} : \mathbf{X} = n_r \mathbf{v}_r, n_r \in \mathbb{Z}, r = 1, 2\} \in \mathbb{R}^2$, being $\mathbf{v}_r = v_r^j \mathbf{e}_j$, $j = 1, 2$ the in-plane independent periodicity vectors. The dynamic balance equations of the infinite metamaterial, in transformed Laplace space, are obtained in the context of in-plane linear theory as

$$\frac{\partial \widehat{\sigma}_{ij}}{\partial x_j} + \widehat{b}_i = \rho s^2 \widehat{u}_i, \quad (1)$$

where $\widehat{\sigma}_{ij}$ are the in-plane stress components, \widehat{u}_i are the in-plane displacement components, \widehat{b}_i and ρ are the transformed source term and the mass density, respectively, s is the complex Laplace variable and x_j are the components of the in-plane position vector $\mathbf{x} = x_j \mathbf{e}_j$, $j = 1, 2$. In transformed Laplace space, the constitutive relations read

$$\widehat{\sigma}_{ij} = C_{ijkl}^\diamond(s) \frac{\partial \widehat{u}_k}{\partial x_l}, \quad (2)$$

being C_{ijkl}^\diamond the components of the constitutive tensor. By substituting (2) in (1), the dynamic equation results

$$\frac{\partial}{\partial x_j} \left(C_{ijkl}^\diamond(s) \frac{\partial \widehat{u}_k}{\partial x_l} \right) + \widehat{b}_i - \rho s^2 \widehat{u}_i = 0. \quad (3)$$

Both constitutive tensors and the mass density are \mathfrak{A} -periodic fulfilling the following relations

$$\begin{aligned} C_{ijkl}^\diamond(\mathbf{x} + n_r \mathbf{v}_r, s) &= C_{ijkl}^\diamond(\mathbf{x}, s), \\ \rho(\mathbf{x} + n_r \mathbf{v}_r) &= \rho(\mathbf{x}), \quad \forall \mathbf{x} \in \mathfrak{A}. \end{aligned} \quad (4)$$

Concerning the constitutive tensor components C_{ijkl}^\diamond , it stands to reason that those related to the linear elastic phases are s -independent, while those of the shunting piezoelectric phase, polarized along the out-of-plane direction and denoted by EL , are in general s -dependent and, accordingly with (Bacigalupo et al., 2020), take the following form

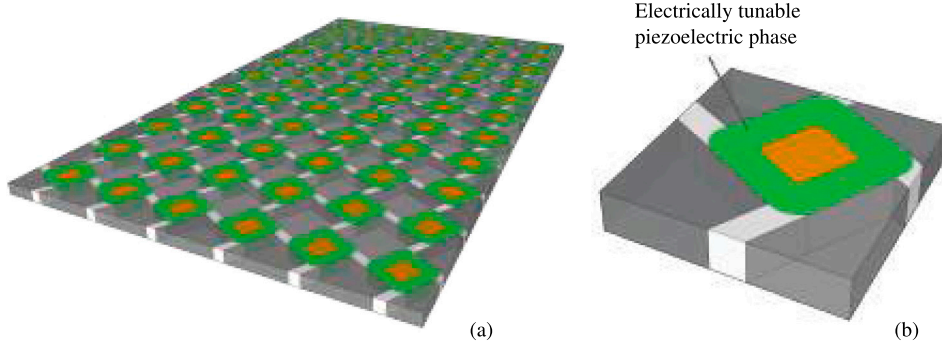


Fig. 1. (a) Portion of a sample periodic shunted metamaterial; (b) Detail of the corresponding Periodic Cell containing the shunted piezoelectric material.

$$C_{ijkl}^{EL}(\lambda(s)) = C_{ijhl} + \frac{e_{ij3}\tilde{e}_{3hl}}{\beta_{33}^{EL}(\lambda(s))} - \left(C_{ij33} + \frac{e_{ij3}\tilde{e}_{333}}{\beta_{33}^{EL}(\lambda(s))} \right) \begin{pmatrix} C_{33hk} + \frac{e_{333}\tilde{e}_{3hl}}{\beta_{33}^{EL}(\lambda(s))} \\ C_{3333} + \frac{e_{333}\tilde{e}_{333}}{\beta_{33}^{EL}(\lambda(s))} \end{pmatrix}, \quad (5)$$

being, with reference to the piezoelectric material, C_{ijhl} the fourth order elasticity tensor components, e_{ij3} the third order stress-charge coupling tensor components and $\tilde{e}_{pq3} = e_{qps}$ its transpose. Moreover, the auxiliary s -dependent function $\beta_{33}^{EL}(\lambda(s)) = \beta_{33}(1 + \lambda(s))$ is introduced, being β_{33} the second order permittivity tensor component and being $\lambda(s) = L^{(P)}Y_{33}^S(s)/(s\beta_{33}A^{(P)})$ the so-called *tuning function* with linear dependence on the generic equivalent shunting admittance $Y_{33}^S(s)$, which is expressed in terms of one or more tuning parameters defining the properties of the generic RLC electrical circuit at hand. Note that in the case of RLC electrical circuits $Y_{33}^S(s)$ turns out to be a rational function of the variable s . In addition $A^{(P)}$ is the in-plane area, and $L^{(P)}$ is the out of plane thickness of the piezoelectric phase. It is worth-noting that the constitutive relation of the shunted piezoelectric material, in Eq. (5), is obtained from an in-plane condensation of those associated to a three-dimensional orthotropic piezoelectric material with polarization along the out-of-plane direction. It results in-plane uncoupled constitutive equations, formally equivalent to the equations of a linearly elastic dielectric material. It also emerges that the elastic tensor of the shunting piezoelectric phase satisfies the major and minor symmetries.

3. Wave propagation and frequency band structure

According to the Floquet–Bloch theory, it is possible to decompose \hat{u}_i as

$$\hat{u}_i = \tilde{u}_i e^{-i(\mathbf{k}\cdot\mathbf{x})}, \quad (6)$$

where \tilde{u}_i are \mathfrak{Q} -periodic Bloch amplitude components, i.e. they fulfil the following relation

$$\tilde{u}_i(\mathbf{x} + n_r \mathbf{v}_r, \mathbf{k}, s) = \tilde{u}_i(\mathbf{x}, \mathbf{k}, s), \quad \forall \mathbf{x} \in \mathfrak{Q}, \quad (7)$$

and $\mathbf{k} = k_j \mathbf{e}_j$, $j = 1, 2$, is the wave vector, spanning all points of the reciprocal space, also known as \mathbf{k} -space. Due to the periodicity of the metamaterial, besides \mathfrak{X} defined in the physical space, it is possible to uniquely identify a periodic reciprocal lattice defined in turn by the discrete subgroup $\mathcal{G} := \{\mathbf{G} : \mathbf{G} = m_s \mathbf{p}_s; m_s \in \mathbb{Z}, s = 1, 2\} \in \mathbb{R}^2$, being $\mathbf{p}_s = p_s^j \mathbf{e}_j$, $j = 1, 2$, the periodicity vectors of the reciprocal lattice that can be determined as

$$\mathbf{p}_\alpha = 2\pi \frac{\mathbf{Q}\mathbf{v}_\beta}{\mathbf{v}_\alpha \cdot \mathbf{Q}\mathbf{v}_\beta}, \quad (8)$$

where \mathbf{Q} is the $\pi/2$ rotation matrix, and $\alpha, \beta = 1, 2$, $\alpha \neq \beta$, so that the scalar product $\mathbf{v}_\alpha \cdot \mathbf{p}_\beta = 2\pi\delta_{\alpha\beta}$ holds. More specifically, also in the reciprocal space it is possible to identify an elementary periodic cell also known as first Brillouin zone \mathfrak{B} . Therefore, by plugging Eq. (6) in (3) after proper manipulations we get

$$\frac{\partial}{\partial x_j} \left(C_{ijh\ell}^\diamond \frac{\partial \tilde{u}_h}{\partial x_\ell} \right) - ik_\ell \left((C_{ijh\ell}^\diamond + C_{i\ell hj}^\diamond) \frac{\partial \tilde{u}_h}{\partial x_j} + \frac{\partial C_{ijh\ell}^\diamond}{\partial x_j} \tilde{u}_h \right) - (k_j k_\ell C_{ijh\ell}^\diamond + \rho s^2 \delta_{ih}) \tilde{u}_h = 0. \quad (9)$$

Due to the \mathfrak{Q} -periodicity of the constitutive tensor components $C_{ijh\ell}^\diamond$, of the mass density ρ and of the Bloch amplitude components \tilde{u}_i , they can be expanded in their Fourier series in terms of \mathbf{G} , defined as

$$\tilde{u}_i = \sum_{\mathbf{n} \in \mathbb{Z}^2} [\tilde{u}_i]_{\mathbf{n}} e^{i\mathbf{G}(\mathbf{n})\cdot\mathbf{x}}, \quad [\tilde{u}_i]_{\mathbf{n}} = \frac{1}{|\mathfrak{Q}|} \int_{\mathfrak{Q}} \tilde{u}_i e^{-i\mathbf{G}(\mathbf{n})\cdot\mathbf{x}} d\mathbf{x}, \quad (10a)$$

$$\rho = \sum_{\mathbf{v} \in \mathbb{Z}^2} [\rho]_{\mathbf{v}} e^{i\mathbf{G}(\mathbf{v})\cdot\mathbf{x}}, \quad [\rho]_{\mathbf{v}} = \frac{1}{|\mathfrak{Q}|} \int_{\mathfrak{Q}} \rho e^{-i\mathbf{G}(\mathbf{v})\cdot\mathbf{x}} d\mathbf{x}, \quad (10b)$$

$$C_{ijh\ell}^\diamond = \sum_{\mathbf{v} \in \mathbb{Z}^2} [C_{ijh\ell}^\diamond]_{\mathbf{v}} e^{i\mathbf{G}(\mathbf{v})\cdot\mathbf{x}}, \quad [C_{ijh\ell}^\diamond]_{\mathbf{v}} = \frac{1}{|\mathfrak{Q}|} \int_{\mathfrak{Q}} C_{ijh\ell}^\diamond e^{-i\mathbf{G}(\mathbf{v})\cdot\mathbf{x}} d\mathbf{x}, \quad (10c)$$

where $\mathbf{n} = (n_1, n_2)$, $\mathbf{v} = (v_1, v_2)$ with $\mathbf{n}, \mathbf{v} \in \mathbb{Z}^2$, and $|\mathfrak{Q}|$ the area of the periodic cell. The derivatives involved in (9) are accordingly defined as

$$\frac{\partial \tilde{u}_i}{\partial x_j} = \sum_{\mathbf{n} \in \mathbb{Z}^2} i(n_r p_r^j) [\tilde{u}_i]_{\mathbf{n}} e^{i\mathbf{G}(\mathbf{n})\cdot\mathbf{x}}, \quad (11a)$$

$$\frac{\partial^2 \tilde{u}_i}{\partial x_\ell \partial x_j} = - \sum_{\mathbf{n} \in \mathbb{Z}^2} (n_r p_r^j)(n_s p_s^\ell) [\tilde{u}_i]_{\mathbf{n}} e^{i\mathbf{G}(\mathbf{n})\cdot\mathbf{x}}, \quad (11b)$$

$$\frac{\partial C_{ijh\ell}^\diamond}{\partial x_j} = \sum_{\mathbf{v} \in \mathbb{Z}^2} i(v_r p_r^j) [C_{ijh\ell}^\diamond]_{\mathbf{v}} e^{i\mathbf{G}(\mathbf{v})\cdot\mathbf{x}}. \quad (11c)$$

Consequently, once we substitute Eqs. (10), (11) into (9), we get the following equation

$$\sum_{\mathbf{n} \in \mathbb{Z}^2} \sum_{\mathbf{v} \in \mathbb{Z}^2} \left(-(v_r p_r^j)(n_s p_s^\ell) [C_{ijh\ell}^\diamond]_{\mathbf{v}} [\tilde{u}_h]_{\mathbf{n}} - (n_r p_r^j)(n_s p_s^\ell) [C_{ijh\ell}^\diamond]_{\mathbf{v}} [\tilde{u}_h]_{\mathbf{n}} + (n_r p_r^j) k_\ell [C_{ijh\ell}^\diamond]_{\mathbf{v}} [\tilde{u}_h]_{\mathbf{n}} + (n_r p_r^j) k_\ell [C_{i\ell hj}^\diamond]_{\mathbf{v}} [\tilde{u}_h]_{\mathbf{n}} + (v_r p_r^j) k_\ell [C_{ijh\ell}^\diamond]_{\mathbf{v}} [\tilde{u}_h]_{\mathbf{n}} - k_j k_\ell [C_{ijh\ell}^\diamond]_{\mathbf{v}} [\tilde{u}_h]_{\mathbf{n}} - [\rho]_{\mathbf{v}} s^2 \delta_{ih} [\tilde{u}_h]_{\mathbf{n}} \right) e^{i(\mathbf{G}(\mathbf{n}) + \mathbf{G}(\mathbf{v}))\cdot\mathbf{x}} = 0. \quad (12)$$

Notice that in general the terms $C_{ijh\ell}^\diamond$, as well as ρ , are piece-wise constant functions, characterizing the different phases of the metamaterial. With specific reference to the constitutive tensor components, the s -dependent coefficients of the Fourier series of the shunted piezoelectric

phase and those s -independent of the elastic phases are denoted by $[C_{ijh\ell}^{\mathfrak{C}}]_n$ and $[C_{ijh\ell}^{\mathfrak{A}\setminus\mathfrak{C}}]_n$, respectively. In this framework, we indicate \mathfrak{C} the region of the periodic cell related to the shunted piezoelectric phase, and $\mathfrak{A}\setminus\mathfrak{C}$ the remaining region related to elastic phases. It follows that the Fourier coefficients of $C_{ijh\ell}^{\diamond}$ becomes

$$[C_{ijh\ell}^{\diamond}]_n = [C_{ijh\ell}^{\mathfrak{A}\setminus\mathfrak{C}}]_n + [C_{ijh\ell}^{\mathfrak{C}}]_n = [C_{ijh\ell}^{\mathfrak{A}\setminus\mathfrak{C}}]_n + r_{ijh\ell}(s)[\chi_{\mathfrak{C}}]_n, \quad (13)$$

where $r_{ijh\ell}$ is a generic rational polynomial function of s which depends on the electric circuit connected to the piezoelectric phase and $\chi_{\mathfrak{C}}$ is the indicator function related to the set (region) \mathfrak{C} , and we include them in Eqs. (12). Therefore, we get the following equations

$$\begin{aligned} \sum_{n \in \mathbb{Z}^2} \sum_{v \in \mathbb{Z}^2} & \left(-(v_r p_j^r)(n_s p_\ell^s) [C_{ijh\ell}^{\mathfrak{A}\setminus\mathfrak{C}}]_v [\tilde{u}_h]_n - (n_r p_j^r)(n_s p_\ell^s) [C_{ijh\ell}^{\mathfrak{A}\setminus\mathfrak{C}}]_v [\tilde{u}_h]_n \right. \\ & + (n_r p_j^r) k_\ell [C_{ijh\ell}^{\mathfrak{A}\setminus\mathfrak{C}}]_v [\tilde{u}_h]_n + (n_r p_j^r) k_\ell [C_{i\ell h j}^{\mathfrak{A}\setminus\mathfrak{C}}]_v [\tilde{u}_h]_n \\ & + (v_r p_j^r) k_\ell [C_{ijh\ell}^{\mathfrak{A}\setminus\mathfrak{C}}]_v [\tilde{u}_h]_n - k_j k_\ell [C_{ijh\ell}^{\mathfrak{A}\setminus\mathfrak{C}}]_v [\tilde{u}_h]_n \\ & + (v_r p_j^r) k_\ell r_{ijh\ell}(s) [\chi_{\mathfrak{C}}]_v [\tilde{u}_h]_n - (v_r p_j^r)(n_s p_\ell^s) r_{ijh\ell}(s) [\chi_{\mathfrak{C}}]_v [\tilde{u}_h]_n \\ & - (n_r p_j^r)(n_s p_\ell^s) r_{ijh\ell}(s) [\chi_{\mathfrak{C}}]_v [\tilde{u}_h]_n + (n_r p_j^r) k_\ell r_{ijh\ell}(s) [\chi_{\mathfrak{C}}]_v [\tilde{u}_h]_n + \\ & + (n_r p_j^r) k_\ell r_{i\ell h j}(s) [\chi_{\mathfrak{C}}]_v [\tilde{u}_h]_n - k_j k_\ell r_{ijh\ell}(s) [\chi_{\mathfrak{C}}]_v [\tilde{u}_h]_n \\ & \left. - [\rho]_v s^2 \delta_{ih} [\tilde{u}_h]_n \right) e^{i(\mathbf{G}(n) + \mathbf{G}(v)) \cdot \mathbf{x}} = 0. \end{aligned} \quad (14)$$

Moreover, by defining the multi-index $\mathbf{m} = \mathbf{v} + \mathbf{n}$, the infinite-dimensional Eq. (14) becomes

$$\begin{aligned} \sum_{n \in \mathbb{Z}^2} \sum_{\mathbf{m} \in \mathbb{Z}^2} & \left(-(m_r - n_r) p_j^r (n_s p_\ell^s) [C_{ijh\ell}^{\mathfrak{A}\setminus\mathfrak{C}}]_{\mathbf{m}-\mathbf{n}} [\tilde{u}_h]_n \right. \\ & - (n_r p_j^r) (n_s p_\ell^s) [C_{ijh\ell}^{\mathfrak{A}\setminus\mathfrak{C}}]_{\mathbf{m}-\mathbf{n}} [\tilde{u}_h]_n - k_j k_\ell [C_{ijh\ell}^{\mathfrak{A}\setminus\mathfrak{C}}]_{\mathbf{m}-\mathbf{n}} [\tilde{u}_h]_n + \\ & + (n_r p_j^r) k_\ell r_{ijh\ell}(s) [\chi_{\mathfrak{C}}]_v [\tilde{u}_h]_n + (n_r p_j^r) k_\ell r_{i\ell h j}(s) [\chi_{\mathfrak{C}}]_{\mathbf{m}-\mathbf{n}} [\tilde{u}_h]_n \\ & + ((m_r - n_r) p_j^r) k_\ell r_{ijh\ell}(s) [\chi_{\mathfrak{C}}]_{\mathbf{m}-\mathbf{n}} [\tilde{u}_h]_n + (n_r p_j^r) k_\ell [C_{ijh\ell}^{\mathfrak{A}\setminus\mathfrak{C}}]_{\mathbf{m}-\mathbf{n}} [\tilde{u}_h]_n \\ & + (n_r p_j^r) k_\ell [C_{i\ell h j}^{\mathfrak{A}\setminus\mathfrak{C}}]_{\mathbf{m}-\mathbf{n}} [\tilde{u}_h]_n + ((m_r - n_r) p_j^r) k_\ell [C_{ijh\ell}^{\mathfrak{A}\setminus\mathfrak{C}}]_{\mathbf{m}-\mathbf{n}} [\tilde{u}_h]_n + \\ & - ((m_r - n_r) p_j^r) (n_s p_\ell^s) r_{ijh\ell}(s) [\chi_{\mathfrak{C}}]_{\mathbf{m}-\mathbf{n}} [\tilde{u}_h]_n \\ & - (n_r p_j^r) (n_s p_\ell^s) r_{ijh\ell}(s) [\chi_{\mathfrak{C}}]_{\mathbf{m}-\mathbf{n}} [\tilde{u}_h]_n + \\ & \left. - k_j k_\ell r_{ijh\ell}(s) [\chi_{\mathfrak{C}}]_{\mathbf{m}-\mathbf{n}} [\tilde{u}_h]_n - [\rho]_{\mathbf{m}-\mathbf{n}} s^2 \delta_{ih} [\tilde{u}_h]_n \right) e^{i\mathbf{G}(\mathbf{m}) \cdot \mathbf{x}} = 0. \end{aligned} \quad (15)$$

In order to write the infinite-dimensional Eq. (15) in a more compact form, we define the infinite-dimensional linear operators \mathbf{A} , \mathbf{B} and $C_{ijh\ell}$, with $i, j, h, \ell = 1, 2$, in terms of the argument $\tilde{\mathbf{u}}$ introduced as

$$\tilde{\mathbf{u}} = \text{col}(\mathbf{u}_1, \mathbf{u}_2) \in \ell_2(\mathbb{Z}^2)^2, \quad (16)$$

where $\mathbf{u}_1, \mathbf{u}_2$ are vectors collecting, respectively, the Fourier coefficients $[\tilde{u}_1]_n, [\tilde{u}_2]_n$, the col operator stacks its vector arguments column-wise into a single column vector, $\ell_2(\mathbb{Z}^2)$ denotes the space of square-summable sequences with two integer indices and $\ell_2(\mathbb{Z}^2)^2$ is $\ell_2(\mathbb{Z}^2) \times \ell_2(\mathbb{Z}^2)$. Consequently, the first operator $\mathbf{A} : \ell_2(\mathbb{Z}^2)^2 \rightarrow \ell_2(\mathbb{Z}^2)^2$ is described in each infinite part as

$$\begin{aligned} \mathbf{A}[\text{col}(\mathbf{u}_1, \mathbf{u}_2)]^{\mathbf{m}1} & = \sum_{n \in \mathbb{Z}^2} \left(-(m_r - n_r) p_j^r (n_s p_\ell^s) [C_{ijh\ell}^{\mathfrak{A}\setminus\mathfrak{C}}]_{\mathbf{m}-\mathbf{n}} [\tilde{u}_h]_n \right. \\ & - (n_r p_j^r) (n_s p_\ell^s) [C_{ijh\ell}^{\mathfrak{A}\setminus\mathfrak{C}}]_{\mathbf{m}-\mathbf{n}} [\tilde{u}_h]_n + \\ & + (n_r p_j^r) k_\ell [C_{ijh\ell}^{\mathfrak{A}\setminus\mathfrak{C}}]_{\mathbf{m}-\mathbf{n}} [\tilde{u}_h]_n + (n_r p_j^r) k_\ell [C_{i\ell h j}^{\mathfrak{A}\setminus\mathfrak{C}}]_{\mathbf{m}-\mathbf{n}} [\tilde{u}_h]_n + \\ & + ((m_r - n_r) p_j^r) k_\ell [C_{ijh\ell}^{\mathfrak{A}\setminus\mathfrak{C}}]_{\mathbf{m}-\mathbf{n}} [\tilde{u}_h]_n \\ & \left. - k_j k_\ell [C_{ijh\ell}^{\mathfrak{A}\setminus\mathfrak{C}}]_{\mathbf{m}-\mathbf{n}} [\tilde{u}_h]_n \right), \end{aligned} \quad (17a)$$

$$\begin{aligned} \mathbf{A}[\text{col}(\mathbf{u}_1, \mathbf{u}_2)]^{\mathbf{m}2} & = \sum_{n \in \mathbb{Z}^2} \left(-(m_r - n_r) p_j^r (n_s p_\ell^s) [C_{2jh\ell}^{\mathfrak{A}\setminus\mathfrak{C}}]_{\mathbf{m}-\mathbf{n}} [\tilde{u}_h]_n \right. \\ & - (n_r p_j^r) (n_s p_\ell^s) [C_{2jh\ell}^{\mathfrak{A}\setminus\mathfrak{C}}]_{\mathbf{m}-\mathbf{n}} [\tilde{u}_h]_n + \\ & + (n_r p_j^r) k_\ell [C_{2jh\ell}^{\mathfrak{A}\setminus\mathfrak{C}}]_{\mathbf{m}-\mathbf{n}} [\tilde{u}_h]_n + (n_r p_j^r) k_\ell [C_{2\ell h j}^{\mathfrak{A}\setminus\mathfrak{C}}]_{\mathbf{m}-\mathbf{n}} [\tilde{u}_h]_n + \end{aligned}$$

$$\begin{aligned} & + ((m_r - n_r) p_j^r) k_\ell [C_{2jh\ell}^{\mathfrak{A}\setminus\mathfrak{C}}]_{\mathbf{m}-\mathbf{n}} [\tilde{u}_h]_n \\ & \left. - k_j k_\ell [C_{2jh\ell}^{\mathfrak{A}\setminus\mathfrak{C}}]_{\mathbf{m}-\mathbf{n}} [\tilde{u}_h]_n \right), \end{aligned} \quad (17b)$$

the second operator $\mathbf{B} : \ell_2(\mathbb{Z}^2)^2 \rightarrow \ell_2(\mathbb{Z}^2)^2$ results

$$\mathbf{B}[\text{col}(\mathbf{u}_1, \mathbf{u}_2)]^{\mathbf{m}1} = - \sum_{n \in \mathbb{Z}^2} [\rho]_{\mathbf{m}-\mathbf{n}} [\tilde{u}_1]_n, \quad (18a)$$

$$\mathbf{B}[\text{col}(\mathbf{u}_1, \mathbf{u}_2)]^{\mathbf{m}2} = - \sum_{n \in \mathbb{Z}^2} [\rho]_{\mathbf{m}-\mathbf{n}} [\tilde{u}_2]_n, \quad (18b)$$

and the last operators $C_{1jh\ell}, C_{2jh\ell} : \ell_2(\mathbb{Z}^2)^2 \rightarrow \ell_2(\mathbb{Z}^2)^2$ are defined as

$$\begin{aligned} C_{1jh\ell}[\text{col}(\mathbf{u}_1, \mathbf{u}_2)]^{\mathbf{m}1} & = \sum_{n \in \mathbb{Z}^2} -((m_r - n_r) p_j^r) (n_s p_\ell^s) r_{ijh\ell}(s) [\chi_{\mathfrak{C}}]_{\mathbf{m}-\mathbf{n}} [\tilde{u}_h]_n \\ & - k_j k_\ell r_{ijh\ell}(s) [\chi_{\mathfrak{C}}]_{\mathbf{m}-\mathbf{n}} [\tilde{u}_h]_n + \\ & - (n_r p_j^r) (n_s p_\ell^s) r_{ijh\ell}(s) [\chi_{\mathfrak{C}}]_{\mathbf{m}-\mathbf{n}} [\tilde{u}_h]_n \\ & + (n_r p_j^r) k_\ell r_{ijh\ell}(s) [\chi_{\mathfrak{C}}]_v [\tilde{u}_h]_n + \\ & + (n_r p_j^r) k_\ell r_{i\ell h j}(s) [\chi_{\mathfrak{C}}]_{\mathbf{m}-\mathbf{n}} [\tilde{u}_h]_n \\ & + ((m_r - n_r) p_j^r) k_\ell r_{ijh\ell}(s) [\chi_{\mathfrak{C}}]_{\mathbf{m}-\mathbf{n}} [\tilde{u}_h]_n, \end{aligned} \quad (19a)$$

$$C_{1jh\ell}[\text{col}(\mathbf{u}_1, \mathbf{u}_2)]^{\mathbf{m}2} = 0, \quad (19b)$$

$$C_{2jh\ell}[\text{col}(\mathbf{u}_1, \mathbf{u}_2)]^{\mathbf{m}1} = 0, \quad (19c)$$

$$\begin{aligned} C_{2jh\ell}[\text{col}(\mathbf{u}_1, \mathbf{u}_2)]^{\mathbf{m}2} & = \sum_{n \in \mathbb{Z}^2} -((m_r - n_r) p_j^r) (n_s p_\ell^s) r_{ijh\ell}(s) [\chi_{\mathfrak{C}}]_{\mathbf{m}-\mathbf{n}} [\tilde{u}_h]_n \\ & - k_j k_\ell r_{ijh\ell}(s) [\chi_{\mathfrak{C}}]_{\mathbf{m}-\mathbf{n}} [\tilde{u}_h]_n + \\ & - (n_r p_j^r) (n_s p_\ell^s) r_{ijh\ell}(s) [\chi_{\mathfrak{C}}]_{\mathbf{m}-\mathbf{n}} [\tilde{u}_h]_n \\ & + (n_r p_j^r) k_\ell r_{ijh\ell}(s) [\chi_{\mathfrak{C}}]_v [\tilde{u}_h]_n + \\ & + (n_r p_j^r) k_\ell r_{i\ell h j}(s) [\chi_{\mathfrak{C}}]_{\mathbf{m}-\mathbf{n}} [\tilde{u}_h]_n \\ & + ((m_r - n_r) p_j^r) k_\ell r_{ijh\ell}(s) [\chi_{\mathfrak{C}}]_{\mathbf{m}-\mathbf{n}} [\tilde{u}_h]_n. \end{aligned} \quad (19d)$$

In this way the compact form of Eqs. (15) is

$$\left(\mathbf{A} + s^2 \mathbf{B} + r_{1jh\ell}(s) C_{1jh\ell} + r_{2jh\ell}(s) C_{2jh\ell} \right) \tilde{\mathbf{u}} = \mathbf{0}, \quad (20)$$

being an infinite-dimensional rational eigenproblem in terms of the eigenvalue s and the eigenvector $\tilde{\mathbf{u}}$, playing the role of complex frequency and polarization vector of the Bloch wave, respectively.

Notice that, by exploiting the symmetries of the tensor $C_{ijh\ell}^{\diamond}$ and, therefore, those of the rational polynomial functions $r_{ijh\ell}$ as well, we can develop the sum over the repeated indices, so that Eq. (20) takes the form

$$\begin{aligned} & \left(\mathbf{A} + s^2 \mathbf{B} + r_{1111}(s) C_{1111} + r_{1211}(s) (3C_{1211} + C_{2111}) \right. \\ & + r_{1212}(s) (2C_{1212} + 2C_{2121}) + r_{1122}(s) (C_{1122} + C_{2211}) \\ & \left. + r_{1222}(s) (C_{1222} + 3C_{2221}) + r_{2222}(s) C_{2222} \right) \tilde{\mathbf{u}} = \mathbf{0}. \end{aligned} \quad (21)$$

In case the rational polynomial $r_{ijh\ell}(s)$ is not in a reduced form we can perform the polynomial division as

$$r_{ijh\ell}(s) = \frac{n_{ijh\ell}(s)}{q_{ijh\ell}(s)} = d_{ijh\ell}(s) + \frac{p_{ijh\ell}(s)}{q_{ijh\ell}(s)}, \quad (22)$$

with $d_{ijh\ell}, p_{ijh\ell}, q_{ijh\ell}$ polynomials in s of a certain degree, and reduced the eigen-problem (21) to the form

$$\left(\mathfrak{P}(\mathbf{A}, \mathbf{B}, C_{ijk\ell}, d_{ijk\ell}(s), s) + \mathfrak{R}(C_{ijk\ell}, p_{ijk\ell}(s), q_{ijk\ell}(s)) \right) \tilde{\mathbf{u}} = \mathbf{0}, \quad (23)$$

where \mathfrak{P} is a polynomial part defined as

$$\begin{aligned} \mathfrak{P} & = \mathbf{A} + s^2 \mathbf{B} + d_{1111}(s) C_{1111} + d_{1211}(s) (3C_{1211} + C_{2111}) \\ & + d_{1212} (2C_{1212} + 2C_{2121}) + d_{1122}(s) (C_{1122} + C_{2211}) \\ & + d_{1222}(s) (C_{1222} + 3C_{2221}) + d_{2222}(s) C_{2222}, \end{aligned} \quad (24)$$

which, if we set as $d = \max\{2, \deg(d_{ijh\ell})\}$, for $i, j, h, \ell = 1, 2$, we may write it as

$$\mathfrak{P} = \mathbf{A}_0 + s \mathbf{A}_1 + \dots + s^d \mathbf{A}_d, \quad (25)$$

and a rational part taking the form

$$\begin{aligned} \mathfrak{R} = & \frac{p_{1111}(s)}{q_{1111}(s)} C_{1111} + \frac{p_{1211}(s)}{q_{1211}(s)} (3C_{1211} + C_{2111}) \\ & + \frac{p_{1212}(s)}{q_{1212}(s)} (2C_{1212} + 2C_{2121}) + \frac{p_{1122}(s)}{q_{1122}(s)} (C_{1122} + C_{2211}) \\ & + \frac{p_{1222}(s)}{q_{1222}(s)} (C_{1222} + 3C_{2221}) + \frac{p_{2222}(s)}{q_{2222}(s)} C_{2222}. \end{aligned} \quad (26)$$

For simplicity in the notation the rational part can be rewritten in compact form as

$$\mathfrak{R} = \sum_{i=1}^6 \frac{p_i(s)}{q_i(s)} D_i, \quad (27)$$

where the assumptions for the s -dependent terms are introduced

$$\begin{aligned} \frac{p_1(s)}{q_1(s)} & := \frac{p_{1111}(s)}{q_{1111}(s)}, & \frac{p_2(s)}{q_2(s)} & := \frac{p_{1211}(s)}{q_{1211}(s)}, & \frac{p_3(s)}{q_3(s)} & := \frac{p_{1212}(s)}{q_{1212}(s)}, \\ \frac{p_4(s)}{q_4(s)} & := \frac{p_{1122}(s)}{q_{1122}(s)}, & \frac{p_5(s)}{q_5(s)} & := \frac{p_{1222}(s)}{q_{1222}(s)}, & \frac{p_6(s)}{q_6(s)} & := \frac{p_{2222}(s)}{q_{2222}(s)}, \end{aligned} \quad (28)$$

as well as the assumption posed for the infinite-dimensional linear operators

$$\begin{aligned} D_1 & := C_{1111}, & D_2 & := 3C_{1211} + C_{2111}, & D_3 & := 2C_{1212} + 2C_{2121}, \\ D_4 & := C_{1122} + C_{2211}, & D_5 & := C_{1222} + 3C_{2221}, & D_6 & := C_{2222}. \end{aligned} \quad (29)$$

Therefore, the infinite dimensional eigen-problem (20) results in the suitable form

$$\left(A_0 + \dots + A_d s^d + \sum_{i=1}^6 \frac{p_i(s)}{q_i(s)} D_i \right) \tilde{u} = 0. \quad (30)$$

4. Truncation and derationalization of the infinite-dimensional rational eigen-problem

The eigenvalue problem (30) is the compact form of the infinite-dimensional algebraic system of Eq. (15). For this reason, an approximate solution of the eigen-problem can be found provided that the system is truncated by restricting the discrete multi-indices m and n to those satisfying $\|m\|_\infty, \|n\|_\infty \leq N$ for a certain $N \in \mathbb{N}^{>0}$, with $\|\cdot\|_\infty$ being the infinity norm. It follows that Eq. (15) becomes

$$\begin{aligned} \sum_{\substack{n \in \mathbb{Z}^2 \\ \|n\|_\infty \leq N}} \sum_{\substack{m \in \mathbb{Z}^2 \\ \|m\|_\infty \leq N}} & \left(-((m_r - n_r)p_r^r)(n_s p_s^s) [C_{ijh\ell}^{\mathfrak{A}\setminus\mathfrak{C}}]_{m-n} [\tilde{u}_h]_n \right. \\ & - (n_r p_r^r)(n_s p_s^s) [C_{ijh\ell}^{\mathfrak{A}\setminus\mathfrak{C}}]_{m-n} [\tilde{u}_h]_n - k_j k_\ell [C_{ijh\ell}^{\mathfrak{A}\setminus\mathfrak{C}}]_{m-n} [\tilde{u}_h]_n + \\ & + (n_r p_r^r) k_\ell r_{ijh\ell}(s) [\chi_{\mathfrak{C}}]_{\nu} [\tilde{u}_h]_n + (n_r p_r^r) k_\ell r_{i\ell h j}(s) [\chi_{\mathfrak{C}}]_{m-n} [\tilde{u}_h]_n \\ & + ((m_r - n_r) p_r^r) k_\ell r_{ijh\ell}(s) [\chi_{\mathfrak{C}}]_{m-n} [\tilde{u}_h]_n + \\ & + (n_r p_r^r) k_\ell [C_{ijh\ell}^{\mathfrak{A}\setminus\mathfrak{C}}]_{m-n} [\tilde{u}_h]_n + (n_r p_r^r) k_\ell [C_{i\ell h j}^{\mathfrak{A}\setminus\mathfrak{C}}]_{m-n} [\tilde{u}_h]_n \\ & + ((m_r - n_r) p_r^r) k_\ell [C_{ijh\ell}^{\mathfrak{A}\setminus\mathfrak{C}}]_{m-n} [\tilde{u}_h]_n + \\ & - ((m_r - n_r) p_r^r)(n_s p_s^s) r_{ijh\ell}(s) [\chi_{\mathfrak{C}}]_{m-n} [\tilde{u}_h]_n \\ & - (n_r p_r^r)(n_s p_s^s) r_{ijh\ell}(s) [\chi_{\mathfrak{C}}]_{m-n} [\tilde{u}_h]_n + \\ & \left. - k_j k_\ell r_{ijh\ell}(s) [\chi_{\mathfrak{C}}]_{m-n} [\tilde{u}_h]_n - [\rho]_{m-n} s^2 \delta_{ih} [\tilde{u}_h]_n \right) e^{iG(m) \cdot x} = 0, \end{aligned} \quad (31)$$

It follows that the infinite operators in the compact form (17)–(19), and (29) are replaced by the corresponding finite dimensional operators, i.e., are replaced by matrices, denoted by the apex (f), so that Eq. (31), by using the same notation in (23) for the corresponding infinite-dimensional problems, takes the form

$$\left(\mathfrak{A}^{(f)} (A^{(f)}, B^{(f)}, C_{ijk\ell}^{(f)}, d_{ijk\ell}(s), s) + \mathfrak{R}^{(f)} (C_{ijk\ell}^{(f)}, p_{ijk\ell}(s), q_{ijk\ell}(s)) \right) \tilde{u}^{(f)} = 0, \quad (32)$$

where the vector $\tilde{u}^{(f)}$ collects the finite-dimensional Fourier coefficients of the Bloch amplitude components. Specifically the finite-dimensional

rational eigen-problem involves matrices of dimension $2M \times 2M$ with $M = (2N + 1)^2$. On the other hand Fourier coefficients associated to the tensors involved in Eqs. (31) are the one related to the multi-indices $m-n$ and, as a consequence, we need to determine $(4N + 1)^2$ coefficients, i.e. the indices whose norm is smaller than $2N$.

It is worth-noting that, dealing with heterogeneous metamaterials, characterized by periodic piece-wise constant functions $C_{ijh\ell}^{\diamond}$, and ρ , their Fourier series exhibit the so-called Gibbs phenomenon. Many studies have been developed on methods to mitigate this phenomenon, exploiting polynomial and rational interpolations (Berrut et al., 2020; De Marchi et al., 2021; Gottlieb and Shu, 1997; Shizgal and Jung, 2003), as well as Fourier series in combination with regularization filters (Jerri, 1998; Bacigalupo et al., 2019). In general these techniques are the more effective the greater is the number of harmonic components necessary to obtain a desired approximation of the periodic functions.

A key point to highlight is that the eigen-problem (32) turns out to be rational and its solution can be obtained resorting to derationalization techniques, able to transform the rational eigen-problem into a polynomial one that in general is simpler to solve. Specifically, since the rational eigen-problem (32) involves rational polynomials expressed in a reduced form, we propose an enhanced derationalization procedure inspired by theoretical investigations on rational eigen-problems detailed in Su and Bai (2011). Specifically it is worth-noting that through this method the rational eigen-problem is transformed in a linear eigen-problem of a slightly larger size, but in general easily solvable. In the case of eigen-problems of large size, this method is computationally advantageous compared to the standard derationalization procedures based on multiplying the rational problem by the product of denominators. On the other hand, when small size problems are taken into account, the two procedures have about the same computational burden. Details on the standard derationalization procedure are included in Vadalá et al. (2021) where the method is exploited to solve a small size eigen-problem.

In this framework, let us consider a generic finite dimensional problem of the same form of (30), that is a rational eigen-problem

$$\left(A_0^{(f)} + \dots + A_d^{(f)} s^d + \sum_{i=1}^k \frac{p_i(s)}{q_i(s)} D_i^{(f)} \right) \tilde{u}^{(f)} = 0, \quad (33)$$

for a generic finite integer number $k \geq 1$, where $A_j^{(f)}$ and $D_i^{(f)}$ are matrices of a certain size $n \times n$, $\tilde{u}^{(f)}$ the related eigenvector of size n and p_i, q_i are polynomials of certain degrees. Notice, moreover, that once we have a polynomial fraction of the type $\frac{p_i(s)}{q_i(s)}$ with $\deg(p_i) < \deg(q_i)$ and $p_i(s) = p_i^{(0)} + \dots + p_i^{(v)} s^v, q_i(s) = q_i^{(0)} + \dots + q_i^{(v)} s^v + s^{v+1}$, it is possible to write it as a product of matrices, in fact (see e.g. Antoulas (2005)) we have that

$$\frac{p_i(s)}{q_i(s)} = (a_i^{(f)})^T (sI_1^{(f)} - E_i^{(f)})^{-1} b_i^{(f)} \quad (34)$$

with

$$a_i^{(f)} = \begin{pmatrix} p_i^{(0)} \\ p_i^{(1)} \\ \vdots \\ p_i^{(v)} \end{pmatrix}^T, \quad E_i^{(f)} = \begin{pmatrix} 0 & 1 & 0 & \dots & 0 \\ 0 & 0 & 1 & \dots & 0 \\ \vdots & \vdots & \vdots & \ddots & \vdots \\ 0 & 0 & 0 & \dots & 1 \\ -q_i^{(0)} & -q_i^{(1)} & -q_i^{(2)} & \dots & -q_i^{(v)} \end{pmatrix}, \quad b_i^{(f)} = \begin{pmatrix} 0 \\ 0 \\ \vdots \\ 0 \\ 1 \end{pmatrix}, \quad (35)$$

and $I_1^{(f)}$ the identity matrix of the same size of $E_i^{(f)}$. Therefore, the rational eigen-problem (33) can be properly specialized by exploiting (34). In this framework we consider the LU decomposition (or rank revealing LU decomposition to reduce the size of the problem) of the matrix $D_i^{(f)}$, i.e. $D_i^{(f)} = L_i^{(f)} U_i^{(f)T}$, so that the rational part of the

eigenvalue problem (33) can be written as follows

$$\begin{aligned} \sum_{i=1}^k \frac{p_i(s)}{q_i(s)} D_i^{(f)} &= \sum_{i=1}^k (\mathbf{a}_i^{(f)})^T (s \mathbf{I}_1^{(f)} - \mathbf{E}_i^{(f)})^{-1} \mathbf{b}_i^{(f)} \mathbf{L}_i^{(f)} (\mathbf{U}_i^{(f)})^T = \\ &= \sum_{i=1}^k \mathbf{L}_i^{(f)} (\mathbf{a}_i^{(f)} (\mathbf{I}_1^{(f)} s - \mathbf{E}_i^{(f)})^{-1} \mathbf{b}_i^{(f)} \mathbf{I}_2^{(f)}) (\mathbf{U}_i^{(f)})^T = \\ &= \sum_{i=1}^k \mathbf{L}_i^{(f)} (\mathbf{I}_2^{(f)} \otimes \mathbf{a}_i^{(f)})^T (s \mathbf{I}_2^{(f)} \otimes \mathbf{I}_1^{(f)} - \mathbf{I}_2^{(f)} \otimes \mathbf{E}_i^{(f)})^{-1} \\ &\quad (\mathbf{I}_2^{(f)} \otimes \mathbf{b}_i^{(f)}) (\mathbf{U}_1^{(f)})^T = \\ &= \mathbf{L}^{(f)} (s \mathbf{F}^{(f)} - \mathbf{G}^{(f)})^{-1} (\mathbf{U}^{(f)})^T, \end{aligned} \tag{36}$$

with $\mathbf{I}_2^{(f)}$ the identity matrix of the size of the matrix $D_i^{(f)}$ (or the rank in the case of the rank revealing decomposition), the symbol \otimes the Kronecker product and the following s -independent matrices are defined

$$\begin{aligned} \mathbf{L}^{(f)} &= [\mathbf{L}_1^{(f)} (\mathbf{I}_2^{(f)} \otimes \mathbf{a}_1^{(f)})^T, \dots, \mathbf{L}_k^{(f)} (\mathbf{I}_2^{(f)} \otimes \mathbf{a}_k^{(f)})^T], \\ \mathbf{F}^{(f)} &= \text{diag}(\mathbf{I}_2^{(f)} \otimes \mathbf{I}_1^{(f)}, \dots, \mathbf{I}_2^{(f)} \otimes \mathbf{I}_1^{(f)}), \\ \mathbf{G}^{(f)} &= \text{diag}(\mathbf{I}_2^{(f)} \otimes \mathbf{E}_1^{(f)}, \dots, \mathbf{I}_2^{(f)} \otimes \mathbf{E}_k^{(f)}), \\ \mathbf{U}^{(f)} &= [\mathbf{U}_1^{(f)} (\mathbf{I}_2^{(f)} \otimes \mathbf{b}_1^{(f)})^T, \dots, \mathbf{U}_k^{(f)} (\mathbf{I}_2^{(f)} \otimes \mathbf{b}_k^{(f)})^T]. \end{aligned} \tag{37}$$

The rational eigen-problem (33) can be thus rewritten in the form

$$\left(\mathbf{A}_0^{(f)} + \dots \mathbf{A}_d^{(f)} s^d + \mathbf{L}^{(f)} (s \mathbf{F}^{(f)} - \mathbf{G}^{(f)})^{-1} (\mathbf{U}^{(f)})^T \right) \tilde{\mathbf{u}}^{(f)} = 0, \tag{38}$$

Finally, a linearization of the problem (38) can be performed by introducing the extra vector variable

$$\mathbf{x}^{(f)} = -(s \mathbf{F}^{(f)} - \mathbf{G}^{(f)})^{-1} (\mathbf{U}^{(f)})^T \tilde{\mathbf{u}}^{(f)} \tag{39}$$

and by setting as

$$\begin{aligned} \mathbf{M}^{(f)} &= \begin{pmatrix} \mathbf{A}_{d-1}^{(f)} & \mathbf{A}_{d-2}^{(f)} & \dots & \mathbf{A}_0^{(f)} & -\mathbf{L}^{(f)} \\ \mathbf{I}^{(f)} & \mathbf{0} & \dots & \mathbf{0} & \\ & \ddots & \ddots & \vdots & \\ & & \mathbf{I}^{(f)} & \mathbf{0} & \\ & & & (\mathbf{U}^{(f)})^T & -\mathbf{G}^{(f)} \end{pmatrix}, \\ \mathbf{N}^{(f)} &= \begin{pmatrix} -\mathbf{A}_d^{(f)} & & & & \\ & \mathbf{I}^{(f)} & & & \\ & & \ddots & & \\ & & & \mathbf{I}^{(f)} & \\ & & & & -\mathbf{F}^{(f)} \end{pmatrix}, \quad \mathbf{y}^{(f)} = \begin{pmatrix} s^{d-1} \tilde{\mathbf{u}}^{(f)} \\ s^{d-2} \tilde{\mathbf{u}}^{(f)} \\ \vdots \\ \tilde{\mathbf{u}}^{(f)} \\ \mathbf{x}^{(f)} \end{pmatrix}, \end{aligned} \tag{40}$$

with $\mathbf{I}^{(f)}$ the identity matrix of the same size of $\mathbf{A}_j^{(f)}$, with $j = 0, \dots, d$, we get that (38) can be rewritten as a linear eigen-problem in the following form

$$(\mathbf{M}^{(f)} - s \mathbf{N}^{(f)}) \mathbf{y}^{(f)} = 0. \tag{41}$$

Therefore the eigen-problem (41) involves matrices of size

$$s_e = 2M \left(P_e + \sum_{i=1}^k \text{deg}(q_i) \right) \times 2M \left(P_e + \sum_{i=1}^k \text{deg}(q_i) \right),$$

with $P_e = \max\{2, \text{deg}(p_i), i = 1, \dots, k\}$. It is worth-noting that this size is much smaller than the size corresponding to matrices involved into the polynomial eigen-problem obtained by exploiting a standard derationalization that is

$$s_s = 2MP_s \times 2MP_s,$$

with $P_s = \max\{2 \prod_{i=0}^k \text{deg}(q_i), \text{deg}(p_j) \prod_{i=0}^k \text{deg}(q_i), j = 1, \dots, k\}$. It emerges that the enhanced derationalization procedure here proposed turns out to be very effective since it requires the treatment of matrices of reduced size. The determination of both the eigenvalues and eigenvectors entails a lower computational burden.

Note that the proposed enhanced derationalization method can also be exploited to study wave propagation in periodic viscoelastic materials where the relaxation kernel is expressed in terms of Prony series. In fact, even in these cases the propagation is governed by rational eigen-problems and this procedure is all the more convenient, compared to standard derationalization techniques, the greater is the number of Prony series terms to be considered for the constitutive characterization of the viscoelastic material.

5. An example of RLC series circuit

Let us consider the case of a metamaterial with a piezoelectric phase characterized by in-plane cubic symmetry and out-of-plane polarized, that is connected in parallel to a RLC series electrical circuit. It results that the non vanishing constitutive tensor components C_{ijkl}^{EL} , introduced in Eq. (5), are in general s dependent, except for the component C_{1212}^{EL} . Therefore, the only rational polynomials involved in (22) are $r_{1111}(s) = r_{2222}(s)$ and $r_{1122}(s)$.

For the considered electrical circuit, the equivalent shunting admittance, first reported in Section 2, specializes in the following form

$$Y_{33}^S(s) = \frac{1}{R_S + sL_S + (sC_S)^{-1}} = \frac{sC_S}{sC_S R_S + s^2 C_S L_S + 1}, \tag{42}$$

being C^S the capacitance, R^S the resistance and L^S is the inductance characterizing the electrical circuit. The related dimensionless tuning function turns out to be

$$\lambda(s) = \frac{L^{(P)} Y_{33}^S(s)}{s \beta_{33} A^{(P)}} = \frac{L^{(p)}}{\beta_{33} A^{(P)}} \frac{C_S}{s C_S R_S + s^2 C_S L_S + 1}. \tag{43}$$

For the sake of convenience Eq. (43) can be expressed in terms of the dimensionless complex frequency $\sigma = s/s_r$ as

$$\lambda(\sigma) = \frac{\lambda_S}{\lambda_S(\sigma \alpha_S + \sigma^2 \beta_S) + 1}, \tag{44}$$

where the control parameters λ_S , α_S , and β_S are dimensionless capacitance, resistance, and inductance, respectively, defined as follows

$$\lambda_S = \frac{C_S}{C_{S_r}} = \frac{L^{(p)}}{\beta_{33} A^{(P)}} C_S, \quad \alpha_S = s_r C_{S_r} R_S, \quad \beta_S = s_r^2 C_{S_r} L_S. \tag{45}$$

Note that λ_S corresponds to the value of the tuning function $\lambda(\sigma)$ evaluated for $\sigma = 0$. Therefore, for the piezoelectric shunted material, the auxiliary s -dependent function β_{33}^{EL} takes the form

$$\begin{aligned} \beta_{33}^{EL} &= \beta_{33} (1 + \lambda(\sigma)) = \beta_{33} \left(1 + \frac{\lambda_S}{\lambda_S(\sigma \alpha_S + \sigma^2 \beta_S) + 1} \right) = \\ &= \beta_{33} \left(\frac{\lambda_S(\sigma \alpha_S + \sigma^2 \beta_S) + 1 + \lambda_S}{\lambda_S(\sigma \alpha_S + \sigma^2 \beta_S) + 1} \right). \end{aligned} \tag{46}$$

It follows that the constitutive tensor components C_{ijhl}^{EL} detailed in (5) are fully defined in terms of the dimensionless frequency σ as well as in terms of λ_S , α_S , and β_S characterizing the electrical circuit.

Moreover, the non vanishing rational functions in (22) can be expressed in the form (See Box I).

$$r_{1111}(\sigma) = r_{2222}(\sigma) = d_1 + \frac{p_1}{q_1(\sigma)}, \quad r_{1122}(\sigma) = d_4 + \frac{p_4}{q_4(\sigma)}, \tag{47}$$

and the second order polynomials in σ are

$$\begin{aligned} q_1(\sigma) = q_4(\sigma) = q(\sigma) &= \sigma^2 + \frac{\alpha_S}{\beta_S} \sigma + \frac{\beta_{33} C_{3333} \lambda_S + \beta_{33} C_{3333} + e_{333} \tilde{e}_{333}}{\beta_S \beta_{33} C_{3333} \lambda_S + \beta_S e_{333} \tilde{e}_{333} \lambda_S} = \\ &= \sigma^2 + q^{(1)} \sigma + q^{(0)}. \end{aligned} \tag{49}$$

where

$$\begin{aligned}
 d_1 &= \frac{\beta_{33}C_{1111}C_{3333} - \beta_{33}C_{1133}C_{3311} + C_{1111}e_{333}\tilde{e}_{333} - C_{1133}e_{333}\tilde{e}_{311} - C_{3311}e_{113}\tilde{e}_{333} + C_{3333}e_{113}\tilde{e}_{311}}{\beta_{33}C_{3333} + e_{333}\tilde{e}_{333}}, \\
 d_4 &= \frac{\beta_{33}C_{1122}C_{3333} - \beta_{33}C_{1133}C_{3322} + C_{1122}e_{333}\tilde{e}_{333} - C_{1133}e_{333}\tilde{e}_{322} - C_{3322}e_{113}\tilde{e}_{333} + C_{3333}e_{113}\tilde{e}_{322}}{\beta_S\lambda_S(\beta_{33}C_{3333} + e_{333}\tilde{e}_{333})^2}, \\
 p_1 &= -\frac{\beta_{33}(C_{3333}e_{113} - C_{1133}e_{333})(C_{3333}\tilde{e}_{311} - C_{3311}\tilde{e}_{333})}{\beta_S(\beta_{33}C_{3333} + e_{333}\tilde{e}_{333})^2}, \\
 p_4 &= -\frac{\beta_{33}(C_{3333}e_{113} - C_{1133}e_{333})(C_{3333}\tilde{e}_{311} - C_{3322}\tilde{e}_{333})}{\beta_S(\beta_{33}C_{3333} + e_{333}\tilde{e}_{333})^2}, \tag{48}
 \end{aligned}$$

Box I.

Therefore the rational eigen-problem (33) can be expressed in the form

$$(\mathbf{A}_0^{(f)} + \sigma^2 \mathbf{A}_2^{(f)} + \frac{1}{q(\sigma)} (2p_1 \mathbf{D}_1^{(f)} + p_4 \mathbf{D}_4^{(f)})) \tilde{\mathbf{u}}^{(f)} = 0, \tag{50}$$

where $\mathbf{A}_0^{(f)} = \mathbf{A}^{(f)} + 2d_1 \mathbf{D}_1^{(f)} + d_4 \mathbf{D}_4^{(f)}$ and $\mathbf{A}_2^{(f)} = \mathbf{B}^{(f)} s_R^2$. This rational eigen-problem can be tackled by resorting to the enhanced derationalization scheme detailed in Section 4. In fact, the rational part can be rewritten in the following suitable form

$$\begin{aligned}
 \frac{1}{q(\sigma)} &= (1 \quad 0) \left(\sigma \mathbf{I}_1^{(f)} - \begin{pmatrix} 0 & 1 \\ -q^{(0)} & -q^{(1)} \end{pmatrix} \right)^{-1} \begin{pmatrix} 0 \\ 1 \end{pmatrix} \\
 &= (\mathbf{a}^{(f)})^T (\sigma \mathbf{I}_1^{(f)} - \mathbf{E}^{(f)})^{-1} \mathbf{b}^{(f)}. \tag{51}
 \end{aligned}$$

Once we consider the LU decomposition of the matrix $2p_1 \mathbf{D}_1^{(f)} + p_4 \mathbf{D}_4^{(f)}$, the eigen-problem (50) becomes

$$(\mathbf{A}_0^{(f)} + \sigma^2 \mathbf{A}_2^{(f)} + \mathbf{L}^{(f)} (\sigma \mathbf{F}^{(f)} - \mathbf{G}^{(f)})^{-1} \mathbf{U}^{(f)T}) \tilde{\mathbf{u}}^{(f)} = 0, \tag{52}$$

with $\mathbf{L}^{(f)} = \mathbf{L}_1^{(f)} (\mathbf{I}_2^{(f)} \otimes \mathbf{a}^{(f)})^T$, $\mathbf{F}^{(f)} = \mathbf{I}_2^{(f)} \otimes \mathbf{I}_1^{(f)}$, $\mathbf{G}^{(f)} = \mathbf{I}_2 \otimes \mathbf{E}^{(f)}$ and $\mathbf{U}^{(f)} = (\mathbf{I}_2 \otimes \mathbf{b}^{(f)}) \mathbf{U}_1^T$ resulting in a specialization of (38). Finally the eigen-problem (52) is linearized as follows

$$(\mathbf{M}^{(f)} - \sigma \mathbf{N}^{(f)}) \mathbf{y}^{(f)} = 0, \tag{53}$$

where

$$\begin{aligned}
 \mathbf{M}^{(f)} &= \begin{pmatrix} 0 & \mathbf{A}_0^{(f)} & -\mathbf{L}^{(f)} \\ \mathbf{I}^{(f)} & 0 & 0 \\ 0 & \mathbf{U}^{(f)T} & -\mathbf{G} \end{pmatrix}, \quad \mathbf{N}^{(f)} = \begin{pmatrix} -\mathbf{A}_2^{(f)} & 0 & 0 \\ 0 & \mathbf{I}^{(f)} & 0 \\ 0 & 0 & -\mathbf{F}^{(f)} \end{pmatrix}, \\
 \mathbf{y}^{(f)} &= \begin{pmatrix} \sigma \tilde{\mathbf{u}}^{(f)} \\ \tilde{\mathbf{u}}^{(f)} \\ \mathbf{x}^{(f)} \end{pmatrix}, \tag{54}
 \end{aligned}$$

with the vector $\mathbf{x}^{(f)}$ defined in (39).

We remark that the considered enhanced derationalization approach enables one to have a significant reduction of the computational burden with respect to the standard derationalization approach. In fact in the latter case, we would have a polynomial eigen-problem of degree 4 which would lead to a linear eigenvalue problem involving matrices considerably bigger than those obtained with the combination of the enhanced derationalization approach together with the subsequent linearization procedure.

6. Illustrative example of a tunable metamaterial

We focus on a three phase metamaterial made by the in-plane regular repetition of a periodic cell along two orthogonal periodicity vectors $\mathbf{v}_1 = d\mathbf{e}_1$ and $\mathbf{v}_2 = d\mathbf{e}_2$. The periodic cell \mathfrak{A} is characterized by a central inner circular disk, of radius r , and by a concentric ring of mean radius R and thickness h , both are denoted as material phase 1. Between the disk and the ring, the material phase 2 occupies the

remaining annular region. The periodic cell is complemented by a material phase 3 surrounding the outer ring. We consider both phases 1 and 3 as linear elastic, while the phase 2 is a shunted piezoelectric phase, whose elastic tensor components were denoted by the apex EL in Eq. (5). It follows that, with reference to Eq. (13), the phase 2 occupies the region \mathfrak{C} , as well as phases 1 and 3 occupy the region $\mathfrak{A} \setminus \mathfrak{C}$.

In this context, the constitutive tensor components $C_{ijh\ell}^\diamond$ together with the mass density ρ can be expressed in the form

$$\begin{aligned}
 C_{ijh\ell}^\diamond(\mathbf{x}) &= C_{ijh\ell}^{(3)} + (C_{ijh\ell}^{(1)} - C_{ijh\ell}^{(3)}) \chi_{\|\mathbf{x}\| \leq r_3}(\mathbf{x}) \\
 &\quad + (C_{ijh\ell}^{(2)} - C_{ijh\ell}^{(1)}) \chi_{\|\mathbf{x}\| \leq r_2}(\mathbf{x}) + (C_{ijh\ell}^{(1)} - C_{ijh\ell}^{(2)}) \chi_{\|\mathbf{x}\| \leq r_1}(\mathbf{x}), \\
 \rho(\mathbf{x}) &= \rho^{(3)} + (\rho^{(1)} - \rho^{(3)}) \chi_{\|\mathbf{x}\| \leq r_3}(\mathbf{x}) + (\rho^{(2)} - \rho^{(1)}) \chi_{\|\mathbf{x}\| \leq r_2}(\mathbf{x}) \\
 &\quad + (\rho^{(1)} - \rho^{(2)}) \chi_{\|\mathbf{x}\| \leq r_1}(\mathbf{x}), \quad \forall \mathbf{x} \in \mathfrak{A}, \tag{55}
 \end{aligned}$$

being $r_1 = r$, $r_2 = R - h/2$ and $r_3 = R + h/2$, χ the indicator function and taking $C_{ijh\ell}^{(2)}$. The corresponding Fourier coefficients can be determined in closed form and result, for $\mathbf{n} \neq \mathbf{0}$, as

$$\begin{aligned}
 [C_{ijh\ell}^\diamond]_{\mathbf{n}} &= \frac{1}{|\mathfrak{A}|} \int_{\mathfrak{A}} C_{ijh\ell}^\diamond(\mathbf{x}) e^{-\frac{2\pi}{d} i(\mathbf{n} \cdot \mathbf{x})} d\mathbf{x} = \sum_{j=1}^3 \frac{A_j}{d^2} \int_{\|\mathbf{x}\| \leq r_j} e^{-\frac{2\pi}{d} i(\mathbf{n} \cdot \mathbf{x})} d\mathbf{x} = \\
 &= \sum_{j=1}^3 \frac{A_j \pi (r_j)^2}{d^2} {}_0F_1 \left(; 2; -\frac{(n_1^2 + n_2^2) \pi^2 (r_j)^2}{d^2} \right), \\
 [\rho]_{\mathbf{n}} &= \frac{1}{|\mathfrak{A}|} \int_{\mathfrak{A}} \rho(\mathbf{x}) e^{-\frac{2\pi}{d} i(\mathbf{n} \cdot \mathbf{x})} d\mathbf{x} = \sum_{j=1}^3 \frac{B_j}{d^2} \int_{\|\mathbf{x}\| \leq r_j} e^{-\frac{2\pi}{d} i(\mathbf{n} \cdot \mathbf{x})} d\mathbf{x} = \\
 &= \sum_{j=1}^3 \frac{B_j \pi (r_j)^2}{d^2} {}_0F_1 \left(; 2; -\frac{(n_1^2 + n_2^2) \pi^2 (r_j)^2}{d^2} \right), \tag{56}
 \end{aligned}$$

where $A_1 = C_{ijh\ell}^{(1)} - C_{ijh\ell}^{(2)}$, $A_2 = C_{ijh\ell}^{(2)} - C_{ijh\ell}^{(1)}$, $A_3 = C_{ijh\ell}^{(1)} - C_{ijh\ell}^{(3)}$, $B_1 = \rho^{(1)} - \rho^{(2)}$, $B_2 = \rho^{(2)} - \rho^{(1)}$, $B_3 = \rho^{(1)} - \rho^{(3)}$, and ${}_0F_1$ is a generalized hypergeometric function as defined in Mathai and Saxena (2006) and briefly recalled in Appendix. In the case where $\mathbf{n} = \mathbf{0}$, the coefficients result as

$$\begin{aligned}
 [C_{ijh\ell}^\diamond]_{\mathbf{0}} &= A_0 + \sum_{j=1}^3 A_j \frac{\pi r_j}{d^2}, \\
 [\rho]_{\mathbf{0}} &= B_0 + \sum_{j=1}^3 B_j \frac{\pi r_j}{d^2}, \tag{57}
 \end{aligned}$$

where $A_0 = C_{ijh\ell}^{(3)}$ and $B_0 = \rho^{(3)}$.

As a remark, we underline that matrices involved in the eigen-problem (41), including the Fourier coefficients in (56), are in general dense matrices, so that a convenient linearization of the generic multi-index m appearing in the finite-dimensional Fourier coefficients can be useful for the sake of computational efficiency. More specifically, the 2D-indices labelled in spiral order as in Fig. 2a are rectified into 1D-indices as done in Fig. 2b, where at the left and at the right of point P_0 are ordered even and odd indices, respectively. Furthermore,

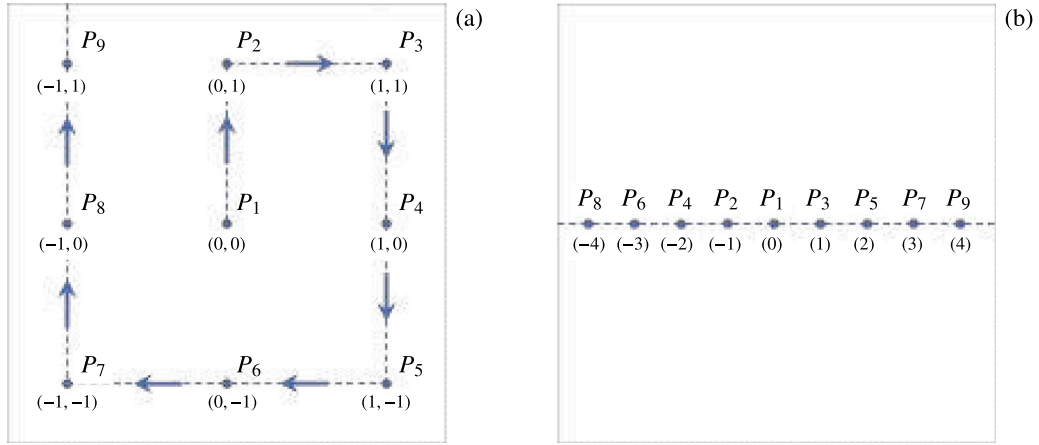


Fig. 2. (a) Spiral ordering of points identified by the 2D-index $m = (m_1, m_2)$; (b) Linear ordering of the 1D-index $m = (m_1)$ as a result of the linearization procedure.

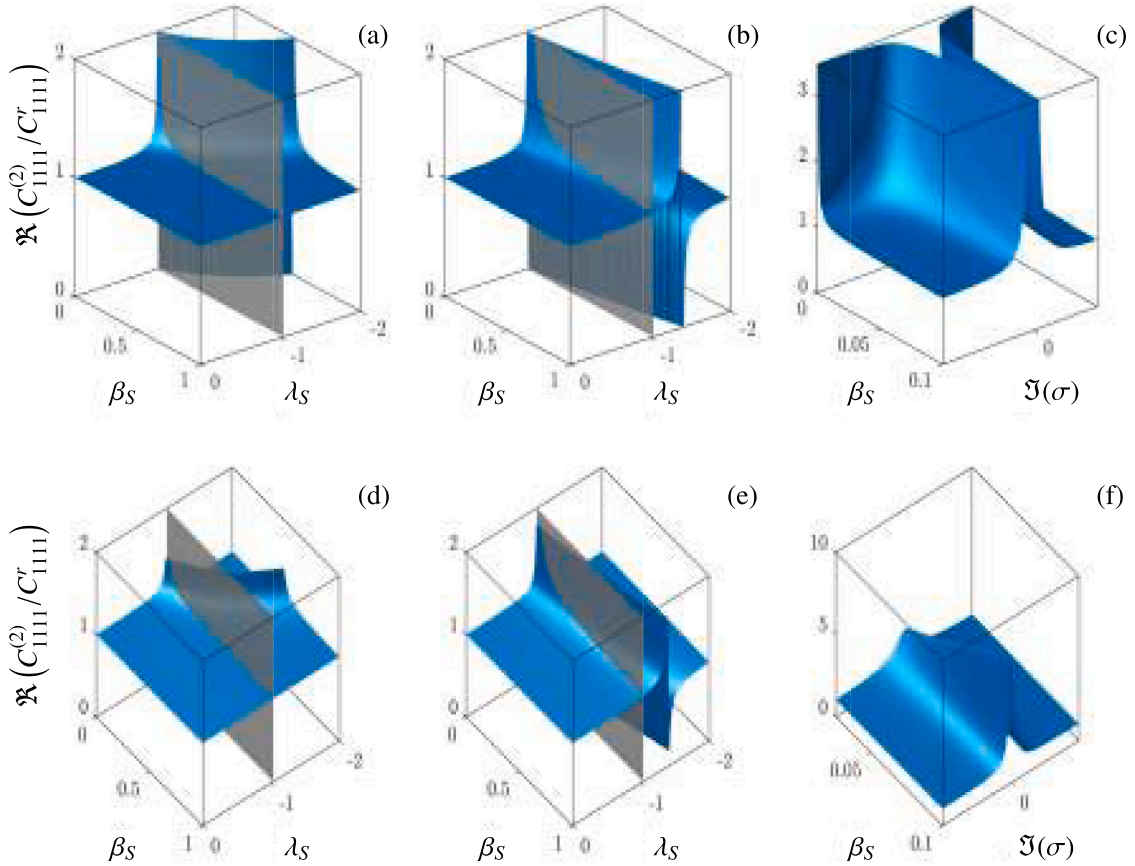


Fig. 3. A set of 3D surface plots of $\Re(C_{1111}^{(2)}(\lambda_S, \alpha_S, \beta_S, \cdot))$ in the parameters space.

note that the multi-index linearization procedure can be favourably exploited also in the consistent truncation of the infinite-dimensional rational eigen-problem.

Finally, in order to assess the minimum required truncation order, a proper convergence analysis is required as the dimension of the linear operators of the truncated eigen-problem increases. All numerical experiments shown in the next sessions are obtained with converged truncation orders.

6.1. Numerical results

We refer to the three-phase metamaterial introduced in Section 6 to test the proposed enhanced derationalization procedure. The phase 1, related to the internal disk together with the outer ring, is made of steel with $E^{(1)}=210$ GPa, $\nu^{(1)}=0.3$ and mass density $\rho^{(1)}=7500$ kg/m³. The second elastic phase, namely phase 3, is made of a passive polymer materials whose commercial name is EPO-TEK[®]301, with $E^{(3)}=3.6$

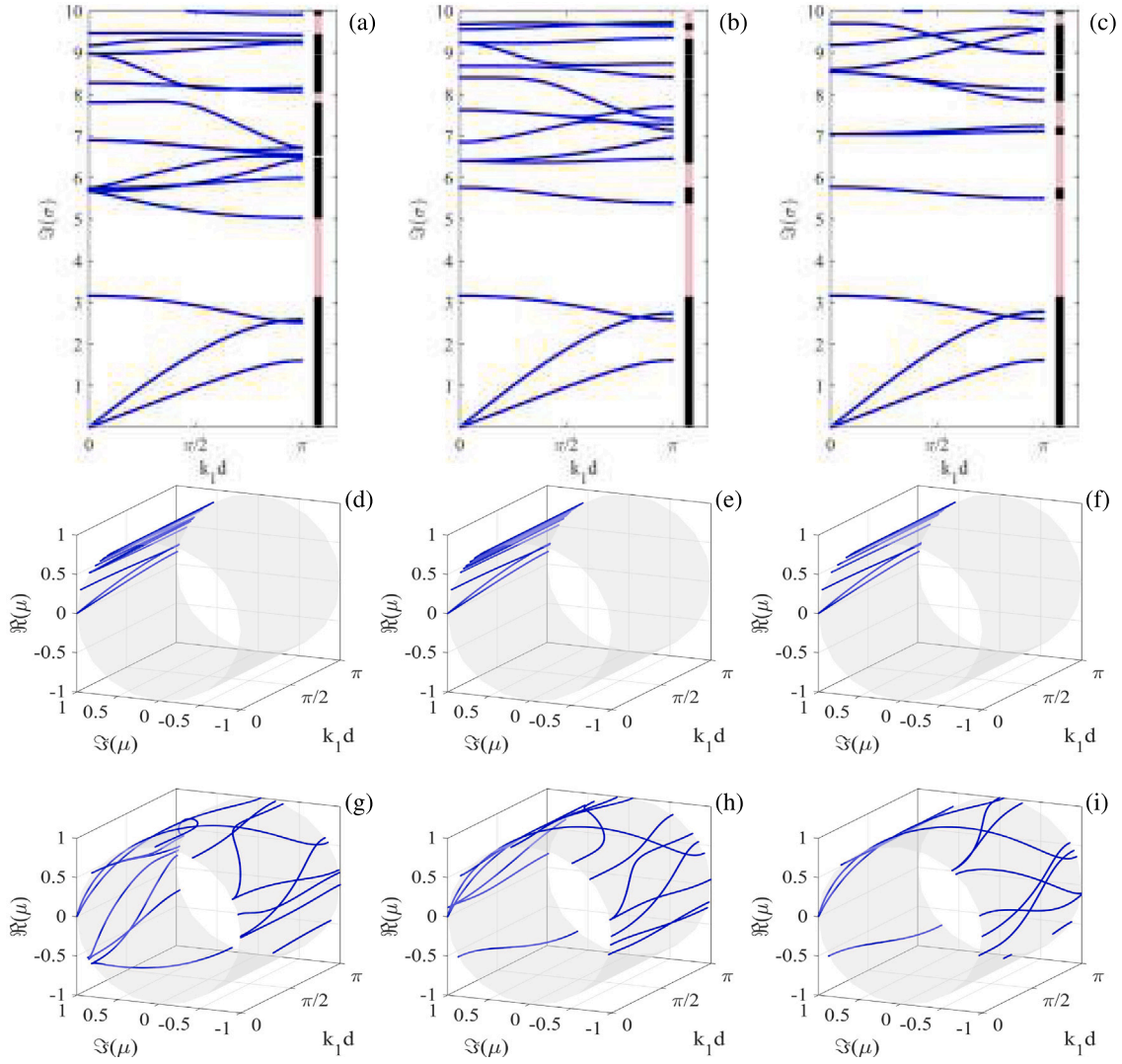


Fig. 4. Dispersion curves for $\alpha_S = 0$, and $\lambda_S = \lambda_R$ as β_S varies. (a), (b), (c) Floquet–Bloch spectra together with their frequency band structure for $\beta_S = 10^{-i}$, $i = 3, 4, 5$, respectively. (d), (e), (f) dispersion curves in terms of μ on the unit cylinder for $\tau=0.1$; (g), (h), (i) dispersion curves in terms of μ on the unit cylinder for $\tau=1$.

GPa, $\nu^{(3)}=0.35$, and mass density $\rho^{(3)}=1150$ kg/m³, as in [Lee et al. \(2014\)](#). As it is well known in the case here considered of plane stress, both these elastic phases are characterized by four non-vanishing components of the elasticity tensor, defined as $C_{1111}^{(j)} = C_{2222}^{(j)} = E^{(j)}/(1 - (\nu^{(j)})^2)$, $C_{1122}^{(j)} = \nu^{(j)}E^{(j)}/(1 - (\nu^{(j)})^2)$, $C_{1212}^{(j)} = E^{(j)}/2(1 - (\nu^{(j)})^2)$, with $j = 1, 3$.

Finally the phase 2, associated to the shunted piezoelectric material, is obtained by connecting a Polyvinylidene fluoride internal ring to a RLC series electrical circuit. The 3D electro-mechanical properties of PVDF, polarized along the out-of-plane \mathbf{e}_3 direction, are taken from [Iyer and Venkatesh \(2014\)](#) and are listed below. Specifically, the non vanishing components of the elasticity tensor are $C_{1111} = C_{2222} = 4.84 \cdot 10^9$ Pa, $C_{3333} = 4.63 \cdot 10^9$ Pa, $C_{1122} = 2.72 \cdot 10^9$ Pa, $C_{1133} = C_{2233} = 2.22 \cdot 10^9$ Pa, $C_{1212} = 1.06 \cdot 10^9$ Pa, $C_{1313} = C_{2323} = 5.26 \cdot 10^7$ Pa. The non vanishing components of the stress-charge coupling tensor are $e_{113} = e_{223} = -1.999 \cdot 10^{-3}$ C/m², $e_{311} = e_{322} = 4.344 \cdot 10^{-3}$ C/m², $e_{333} = -1.099 \cdot 10^{-1}$ C/m². The set of components is complemented by the non vanishing components of the dielectric permittivity tensor, i.e. $\beta_{11} = \beta_{22} = 6.641 \cdot 10^{-11}$ C/Vm, and $\beta_{33} = 7.083 \cdot 10^{-11}$ C/Vm. Moreover the mass density is $\rho^{(2)} = 1780$ kg/m³.

As it emerges from Section 5, by modifying the tuning parameters, i.e. the dimensionless capacitance λ_S , resistance α_S , and inductance

β_S , the constitutive tensor components, detailed in (5), are changed in turn. In this respect, with the aim of better understanding the influence of tuning parameters on the equivalent elastic response of the shunting piezoelectric phase, in [Fig. 3](#) the real part of the elastic tensor component $C_{1111}^{(2)}$, i.e. $\Re(C_{1111}^{(2)}(\lambda_S, \alpha_S, \beta_S, \sigma))$, normalized with respect to the σ -independent component $C_{1111}^r = C_{1111}^{(2)}(\lambda_S = 0, \alpha_S = 0, \beta_S = 0)$, is shown in the parameters space and in the complex frequency domain.

In particular, the three plots on the first row refer to $\alpha_S = 0$, that is the case of a non-dissipative electrical circuit. In [Fig. 3\(a\)](#) the 3D surface plot of $\Re(C_{1111}^{(2)}/C_{1111}^r)$ is shown versus β_S and λ_S , assuming $\Re(\sigma) = 0$ and $\Im(\sigma) = 1$. The grey shaded plane corresponds to the σ -independent resonance value of the tuning parameter $\lambda_S \equiv \lambda_R = -(C_{3333}\beta_{33} + e_{333}^2)/(C_{3333}\beta_{33})$, introduced in [Bacigalupo et al. \(2020\)](#), occurring in the case of a purely capacitive circuit characterized by $\alpha_S = \beta_S = 0$. Analogously, in [Fig. 3\(b\)](#) the 3D surface plot of $\Re(C_{1111}^{(2)}/C_{1111}^r)$ is shown versus β_S and λ_S , $\Re(\sigma) = 0$ and $\Im(\sigma) = 1/2$. In addition, in [Fig. 3\(c\)](#) the 3D surface plot of $\Re(C_{1111}^{(2)}/C_{1111}^r)$ is shown versus β_S and $\Im(\sigma)$ assuming $\lambda_S = \lambda_R$.

On the other hand, the three plots on the second row, i.e. (d), (e) and (f), are the same as for the first row, but referring to a dissipative circuit with $\alpha_S = 1/80$. It emerges that in the plots shown in the first row, corresponding to the non-dissipative circuit, singularities appear,

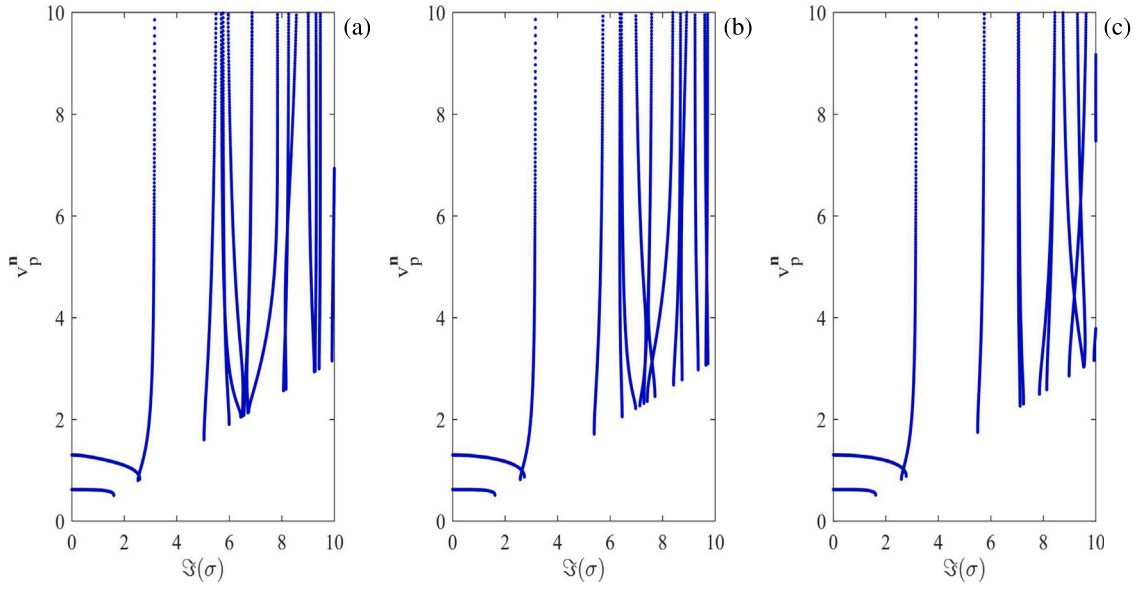


Fig. 5. Dimensionless magnitude v_p^n , with $\mathbf{n} = \mathbf{e}_1$, of the phase velocity vector versus $\Im(\sigma)$ for $\alpha_S = 0$, $\lambda_S = \lambda_R$ and $\beta_S = 10^{-i}$, $i = 3, 4, 5$.

located on the points pertaining to the following implicit function

$$F(\lambda_S, \alpha_S, \beta_S, \Im(\sigma)) = (A(\alpha_S, \beta_S, \Im(\sigma)) \lambda_S^2 + B(\alpha_S, \beta_S, \Im(\sigma)) \lambda_S + C(\alpha_S, \beta_S, \Im(\sigma))) = 0, \quad (58)$$

where the auxiliary coefficients are defined as

$$\begin{aligned} A(\alpha_S, \beta_S, \Im(\sigma)) &= D_1 D_2 \beta_S^2 \Im(\sigma)^4 + (D_1 D_2 \alpha_S^2 + D_1 D_3 \beta_S) \Im(\sigma)^2 \\ &\quad + D_1 C_{3333}^2 \beta_{33}^2, \\ B(\alpha_S, \beta_S, \Im(\sigma)) &= -2 D_1 D_2 \beta_S \Im(\sigma)^2 - D_1 D_3, \\ C(\alpha_S, \beta_S, \Im(\sigma)) &= D_1 D_2, \end{aligned} \quad (59)$$

with

$$\begin{aligned} D_1 &= C_{1111} C_{3333} \beta_{33} + e_{333}^2 C_{1111} - C_{1133}^2 \beta_{33} - 2 e_{113} e_{333} C_{1133} + e_{113}^2 C_{3333}, \\ D_2 &= C_{3333}^2 \beta_{33}^2 + 2 C_{3333} \beta_{33} e_{333}^2 + e_{333}^4, \\ D_3 &= -2 C_{3333}^2 \beta_{33}^2 - 2 C_{3333} \beta_{33} e_{333}^2. \end{aligned} \quad (60)$$

On the other hand, observing the corresponding behaviour in the case of a dissipative circuit, i.e. the second row of the figure, it is noted that the discontinuities turn into peaks. Moreover, in either event of non dissipative or dissipative circuit, it is worth mentioning that for $\Re(\sigma) = 0$ as $\Im(\sigma)$ tends to zero the singularity/peak tends to move and lie on the grey plane.

In Figs. 4(a), (b) and (c), Floquet–Bloch spectra are plot in terms of the dimensionless frequency $\sigma = s/s_r$, with $s_r = d^{-1} \sqrt{C_{3333}^{PVDF} / \rho^{PVDF}}$ a reference frequency, versus the dimensionless abscissa $k_1 d$ considering $\alpha_S = 0$ and $\lambda_S = \lambda_R$ for different values of β_S . In this case of non-dissipative circuit shunting the piezoelectric phase the complex frequencies have zero real part. Moving from the highest value of $\beta_S = 10^{-3}$ (Fig. 4(a)), to $\beta_S = 10^{-4}$ (Fig. 4(b)), up to $\beta_S = 10^{-5}$ (Fig. 4(c)) it emerges that the first band gap becomes noticeably wider, as well as overall the spectra tend to get less dense and new band gaps form at higher frequencies. Other parameters being equal, reducing the β_S parameter results in a better filtering effect. Additionally, the frequency band structures in terms of stop and pass band amplitudes are plotted in the right part of Figs. 4(a), (b), (c). A further representation is shown in Figs. 4(d)–(i) displaying dispersion curves in terms of real and imaginary parts of $\mu = \exp(\sigma\tau)$ versus $k_1 d$ for $\alpha = 0$ and $\lambda_S = \lambda_R$ and a fixed value of the dimensionless time $\tau = t s_r$, where t is the time variable. More specifically, in Figs. 4(d)–(f) the dimensionless time is fixed to $\tau = 0.1$, at the same values of β_S as the upper row.

Analogously, in Figs. 4(g)–(i) the dimensionless time is fixed to $\tau = 1$. In the considered non dissipative case ($\alpha_S = 0$) it is worth-noting that spectra are located on the unit cylinder. As τ increases, spectra become less narrow and they wrap almost completely on the unit cylinder. In the considered cases, the control parameter β_S is varying in the grey shaded plane shown in Fig. 3(a),(b).

Let us now consider the phase velocity vector $\mathbf{v}_p(\mathbf{n}) = (\Im(s)/k) \mathbf{n}$ of the wave travelling in the direction $\mathbf{n} := \mathbf{k} / \|\mathbf{k}\|_2$ with corresponding wave number $k := \|\mathbf{k}\|_2$. Consistently the dimensionless magnitude of \mathbf{v}_p can be defined as $v_p^n := \|\mathbf{v}_p(\mathbf{n})\|_2 / (s_r d) = \Im(s) / (k d)$. Specifically, in Fig. 5 the quantity $v_p^{e_1} = \Im(s) / (k_1 d)$ specialized when $\mathbf{n} = \mathbf{e}_1$ is plot in terms of $\Im(\sigma)$ for $\alpha_S = 0$, and $\lambda_S = \lambda_R$ as β_S varies. It emerges that, irrespective of β_S , the first two curves at the lowest frequencies are associated with the corresponding two acoustic branches in Figs. 4(a), (b), (c), respectively. As expected finite values of the phase velocities are found in this case. In addition, the remaining curves at higher frequencies are associated with optical branches of the Floquet–Bloch spectra, exhibiting vertical asymptotes corresponding to infinite velocity values. As a further remark, pass and stop bands are recognizable along abscissas, as well as it emerges their tunability as parameter λ varies.

Fig. 6 reports dispersion curves for the dimensionless resistance $\alpha_S = 10^{-5}$ considering $\lambda_S = \lambda_R$ and $\beta_S = 10^{-i}$, $i = 3, 4, 5$ from the first to the third column. Due to the presence of this non vanishing dissipative control parameter α_S , the complex Floquet–Bloch spectra are characterized by both non vanishing real and imaginary parts of the complex dimensionless frequency versus $k_1 d$, as can be observed in Figs. 6(a),(b),(c). It is also evident that, as β_S decreases, increasing values of $-\Re(\sigma)$ are found, i.e. an increasing damping behaviour is exhibited. In fact, in the considered case the control parameter β_S moves on the grey shaded plane shown in Figs. 3(d),(e) and it emerges that as β_S tends to vanish the real part of the constitutive tensor components of the shunted piezoelectric material exhibit a peak. In Figs. 6(d)–(i) dispersion curves in terms of real and imaginary parts of $\mu = \exp(i\sigma\tau)$ versus $k_1 d$ for $\alpha_S = 10^{-5}$, $\lambda_S = \lambda_R$ and a fixed value of the dimensionless time $\tau = t s_r$, are shown. The non vanishing dissipative control parameter α_S has a direct effect on the position of the dispersion curves with respect to the unit cylinder. Indeed as τ increases, for fixed β_S values, the dispersion curves do not remain on the unit cylinder as they wrap, but move inwards. Moreover, as β_S decreases in the range

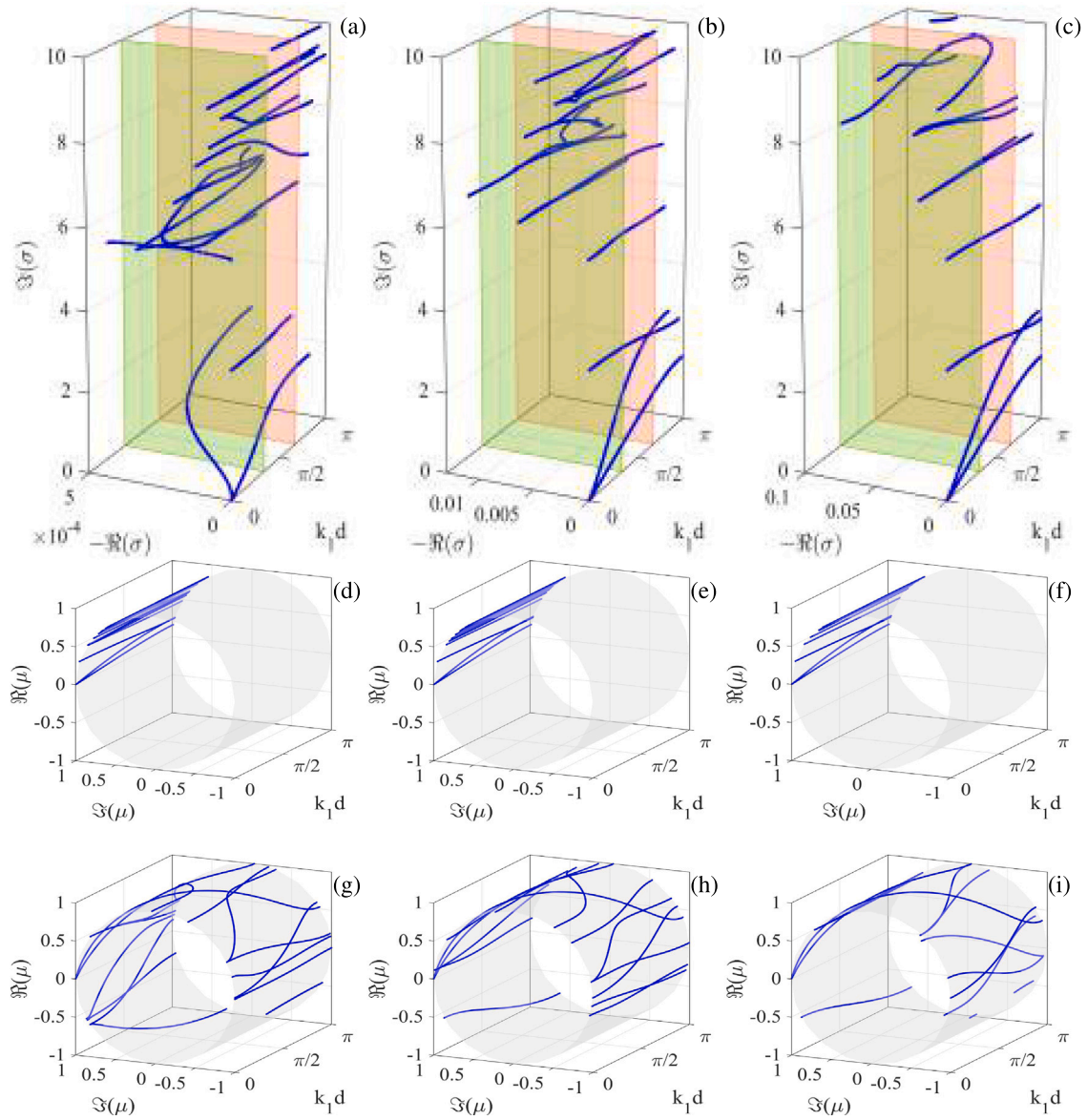


Fig. 6. Dispersion curves for $\alpha_S = 10^{-5}$, and $\lambda_S = \lambda_R$ as β_S varies. (a), (b), (c) Complex Floquet–Bloch spectra for $\beta_S = 10^{-i}, i = 3, 4, 5$, respectively. (d), (e), (f) dispersion curves in terms of μ on the unit cylinder for $\tau=0.1$; (g), (h), (i) dispersion curves in terms of μ on the unit cylinder for $\tau=1$.

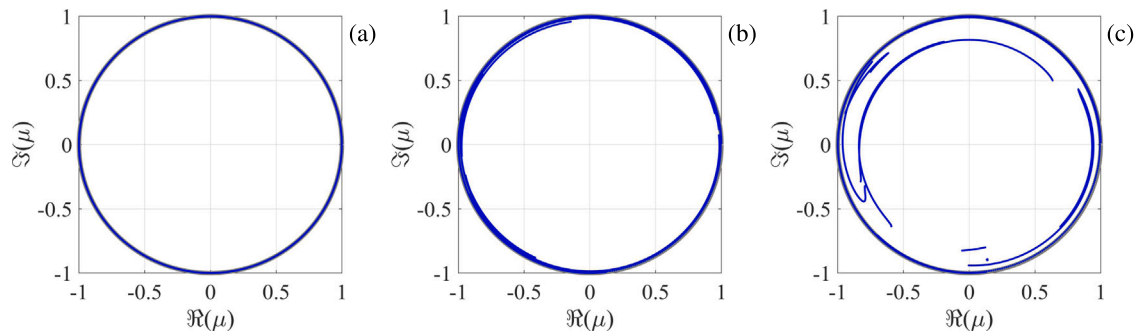


Fig. 7. Dispersion curves in terms of μ on the unit circle for $\tau=1$, $\alpha_S = 10^{-5}$, $\lambda_S = \lambda_R$ as β_S varies. (a), (b) and (c) corresponds to $\beta_S = 10^{-i}, i = 3, 4, 5$, respectively.

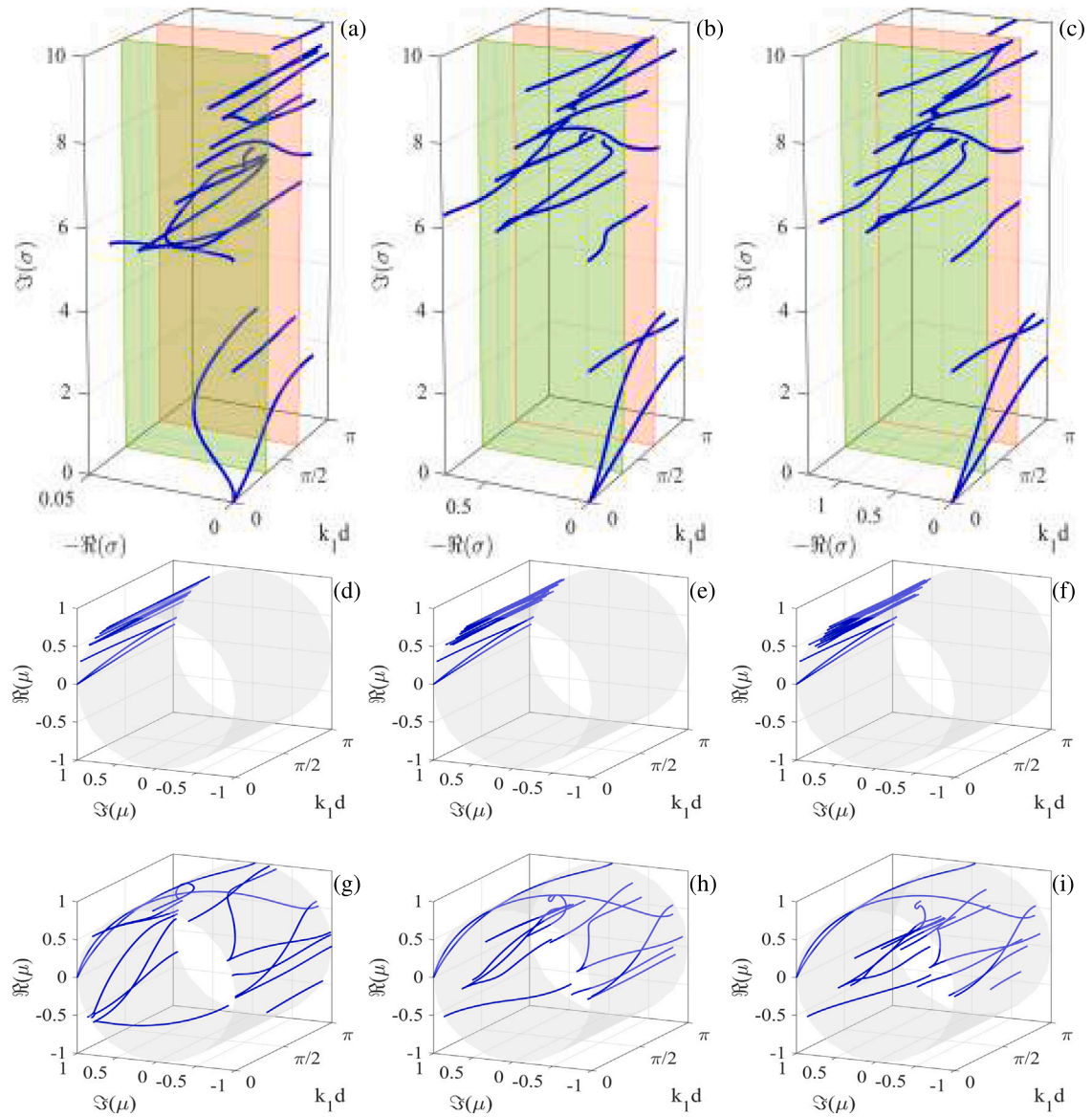


Fig. 8. Dispersion curves for $\alpha_S = 10^{-3}$, and $\lambda_S = \lambda_R$ as β_S varies. (a), (b), (c) Complex Floquet–Bloch spectra for $\beta_S = 10^{-4}$, $i = 3, 4, 5$, respectively. (d), (e), (f) dispersion curves in terms of μ on the unit cylinder for $\tau=0.1$; (g), (h), (i) dispersion curves in terms of μ on the unit cylinder for $\tau=1$.

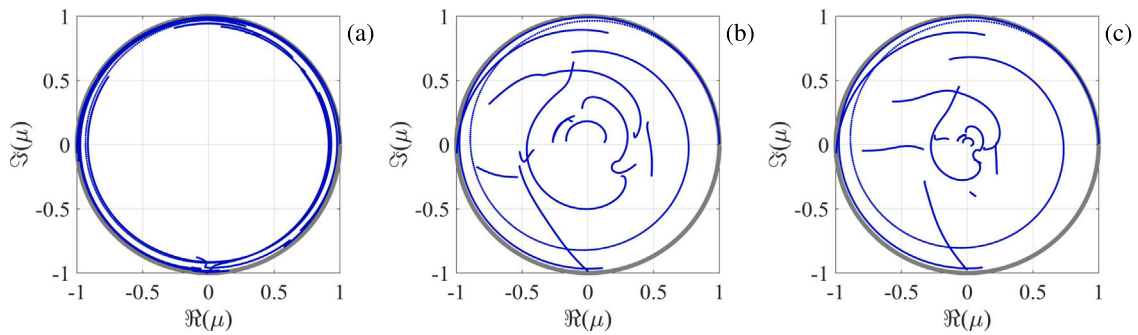


Fig. 9. Dispersion curves in terms of μ on the unit circle for $\tau=1$, $\alpha_S = 10^{-3}$, $\lambda_S = \lambda_R$ as β_S varies. (a), (b) and (c) corresponds to $\beta_S = 10^{-4}$, $i = 3, 4, 5$, respectively.

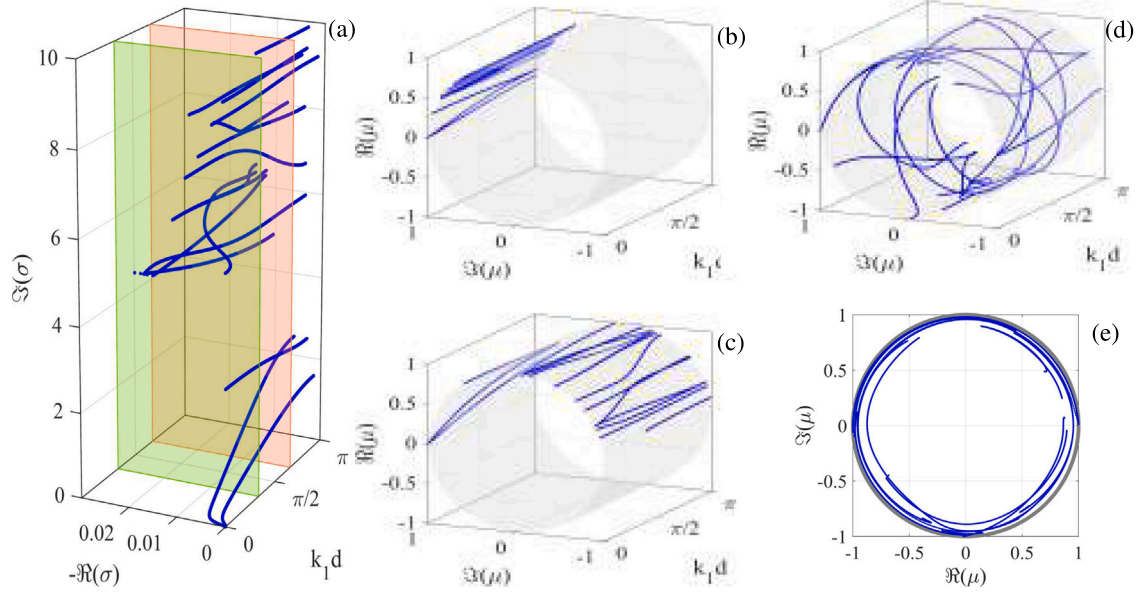


Fig. 10. Dispersion curves for $\alpha_S = 10^{-1}$, and $\lambda_S = \lambda_R$ and $\beta_S = 10^{-3}$. (a) Floquet–Bloch spectrum. (b), (c), (d) dispersion curves in terms of μ on the unit cylinder for $\tau=0.1,1,3$, respectively. (e) front view of the dispersion curves for $\tau=3$.

$\beta_S = 10^{-i}$, $i = 3, 4, 5$ this effect of moving away from the cylinder is increasingly evident as clearly appear in the front views of Fig. 7.

Analogously, Fig. 8 reports dispersion curves for the dimensionless resistance $\alpha_S = 10^{-3}$ considering $\lambda_S = \lambda_R$ and $\beta_S = 10^{-i}$, $i = 3, 4, 5$ from the first to the third column. Again, the Floquet–Bloch spectra are characterized by both non vanishing real and imaginary parts of the complex dimensionless frequency versus $k_1 d$, as can be observed in Fig. 8(a),(b),(c). With respect to these complex spectra it is well evident that, as the beta decreases, branches occupy ever larger areas in the real field. In Figs. 8(d)–(i) dispersion curves in terms of real and imaginary parts of $\mu = \exp(\sigma\tau)$ versus $k_1 d$ for $\alpha_S = 10^{-3}$, $\lambda_S = \lambda_R$ and a fixed value of the dimensionless time $\tau = t_s$, are shown. Also in this case, in Figs. 8(d)–(f) the dimensionless time is fixed to $\tau=0.1$, at the same values of β_S as the upper row. In Figs. 8(g)–(i) the dimensionless time is fixed to $\tau = 1$. A qualitative behaviour similar to Fig. 6 is observed, but in this case the tendency of the curves to go towards the centre of the unit cylinder as β_S decreases is more accentuated, as can be seen in Fig. 9 corresponding to $\tau = 1$.

Furthermore, in Fig. 10 results corresponding to a dimensionless resistance $\alpha_S = 10^{-1}$, $\lambda_S = \lambda_R$ and $\beta_S = 10^{-3}$ are reported. Also in this case, the Floquet–Bloch spectrum is characterized by both real and imaginary parts of the complex dimensionless frequency versus $k_1 d$, as can be seen in Fig. 10(a). In this case Figs. 10(b)–(e) show dispersion curves in terms of real and imaginary parts of $\mu = \exp(\sigma\tau)$ versus $k_1 d$ for $\lambda = \lambda_R$ and a fixed value of the dimensionless time $\tau = t_s$. Fig. 10(b) corresponds to $\tau=0.1$, Fig. 10(c) to $\tau=0.3$ and both Figs. 10(d)–(e) correspond to $\tau=3$. Dispersion curves move away from each other as τ increases, concurrently they do not remain on the unit cylinder as they wrap, but move inwards as clearly emerges from the front view in Fig. 10(e). It can be verified that for this value of α_S unnoticeable differences arise in the spectra as β_S varies.

As a remark, it is important observing that, as expected, a non monotonic damping behaviour is exhibited as α_S increases. In fact, the range of the real part of the dimensionless complex frequency has not a monotonic behaviour as the dissipative control parameter α_S increases, as shown in Arena et al. (2022), Fantoni et al. (2023) and investigated in Figs. 11 and 12. More precisely, the frequency loci as the dimensionless resistance α_S varies are plotted for two discrete values

of the dimensionless abscissa $k_1 d$. In Figs. 11(a), (b), (c) and Figs. 12(a), (b), (c) the 3D plots corresponding to $k_1 d = \pi/3$ and $k_1 d = 2\pi/3$ are shown, respectively, as beta decreases. In addition Figs. 11(d), (e), (f) and 12(d), (e), (f) are a further representation in which the variability of α_S is shown graphically as a logarithmic colour scale.

7. Final remarks

The paper is devoted to the design of tunable mechanical metamaterials conceived for the control of damped elastic wave propagation. The attention is focused on a periodic metamaterial with three phases, two of which are elastic and the last one is piezoelectric and connected in parallel to a tunable dissipative electric circuit. By intervening on the electric circuit it is possible to modify the equivalent stiffness of the piezoelectric phase and, therefore, to obtain a metamaterial whose response spectrum can be modified according to the needs by opening/closing or widening/translating the band gaps. Due to the presence of a dissipative electric circuit, the analysis of wave propagation involves a rational eigenvalue problem, the solution of which is very difficult using both analytical and computational methods available in the literature. In this context, an innovative derationalization technique is herein proposed. The idea is to start from an infinite-dimensional eigenvalue problem, obtained by exploiting the Fourier series decomposition of all the periodic terms, and then apply a truncation. At this point the procedure foresees a LU factorization of the matrix that collects the terms of the rational part of the eigenvalue problem, to then proceed to a subsequent linearization. The proposed method proves to be effective in obtaining the Floquet–Bloch spectra in a reasonable time and achieving a good convergence. The rational eigenvalue problem is solved by slightly increasing the size of the original rational eigenvalue problem and therefore is computationally more efficient than the brute force approach consisting in multiplying the rational eigenvalue problem by the product of the denominators. This technique is successfully applied to the case of a metamaterial shunted to a series RLC circuit with rational admittance. The effects of changing control parameters, i.e. the capacitance, the resistance and the inductance, on the overall dispersive response of the designed metamaterial is investigated and critically commented.

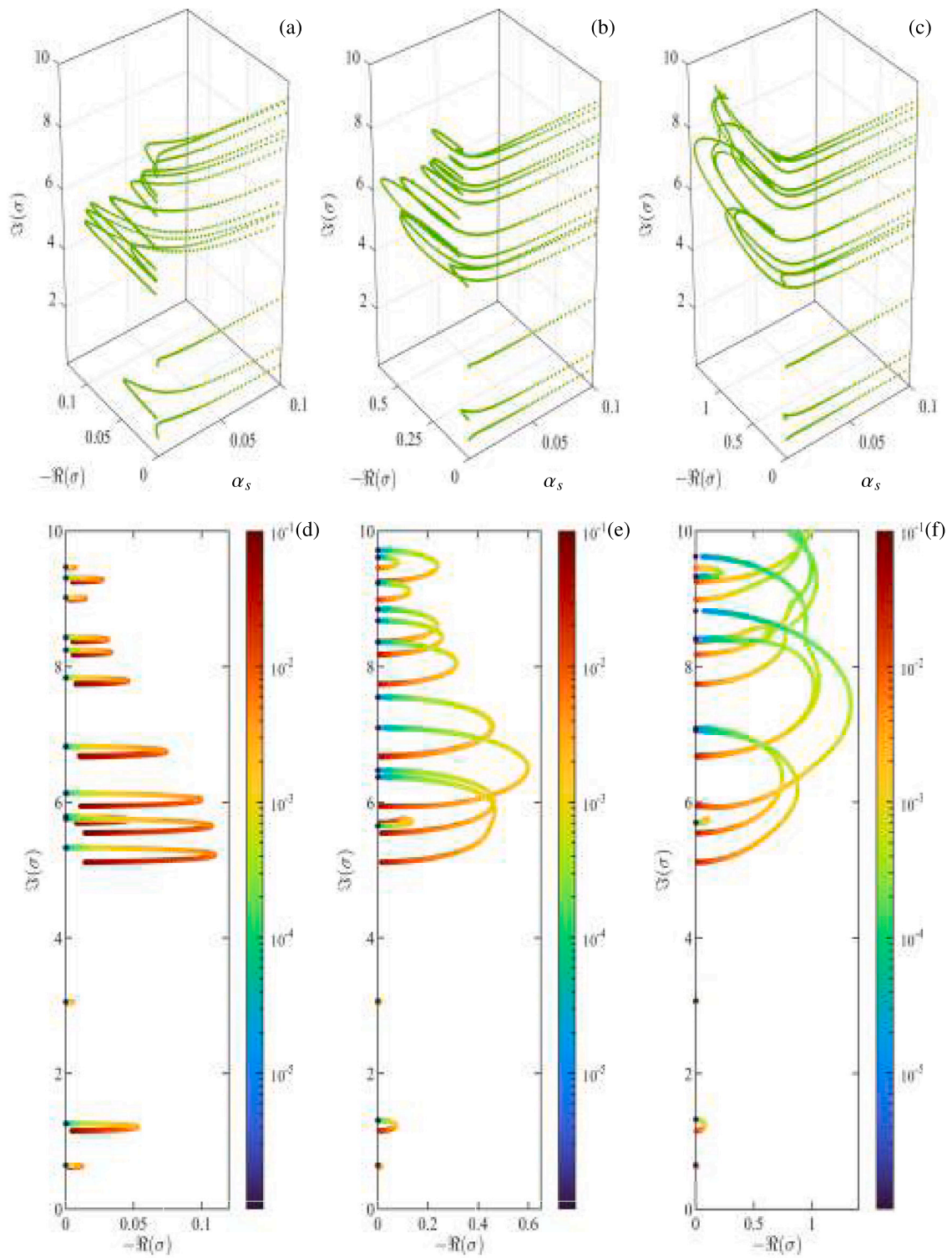


Fig. 11. Loci of the complex frequency for $k_1 d = \pi/3$: (a), (b), (c) 3D plots of real and imaginary parts of the dimensionless complex frequency σ versus α_S for $\beta_S = 10^{-i}$, $i = 3, 4, 5$, respectively; (d), (e), (f) 2D plots of real and imaginary parts of the dimensionless complex frequency σ with α_S shown as a logarithmic colour scale.

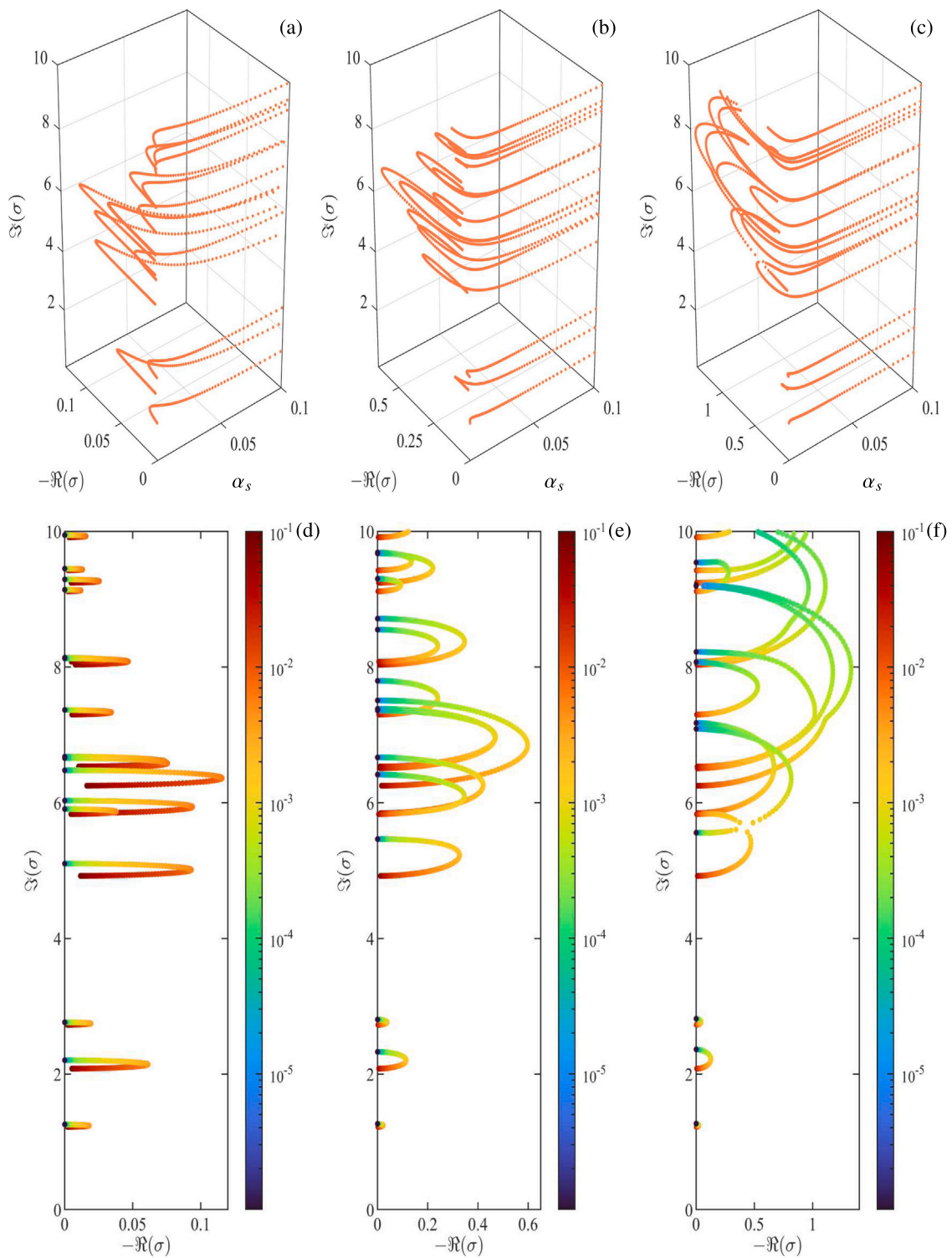


Fig. 12. Loci of the complex frequency for $k_1 d = 2\pi/3$: (a), (b), (c) 3D plots of real and imaginary parts of the dimensionless complex frequency σ versus α_s for $\beta_s = 10^{-i}$, $i = 3, 4, 5$, respectively; (d), (e), (f) 2D plots of real and imaginary parts of the dimensionless complex frequency σ with α_s shown as a logarithmic colour scale.

Declaration of competing interest

The authors declare that they have no known competing financial interests or personal relationships that could have appeared to influence the work reported in this paper.

Data availability

Data will be made available on request.

Acknowledgements

The authors gratefully acknowledge financial support from National Group of Mathematical Physics, Italy (GNFM-IN δ AM), from University of Chieti-Pescara project Search for Excellence Ud'A 2019 and from University of Trento, project UNMASKED 2020. This research has been accomplished within Rete Italiana di Approssimazione (RITA), the thematic group on "Teoria dell'Approssimazione e Applicazioni"(TAA) of the Italian Mathematical Union and with the support of GNCS-IN δ AM.

Appendix. Overview of hypergeometric functions

The hypergeometric function ${}_0F_1$ is a particular case of the generalized hypergeometric series ${}_pF_q(a_1, \dots, a_p; b_1, \dots, b_q; z)$ which is defined as

$${}_pF_q(a_1, \dots, a_p; b_1, \dots, b_q; z) = \sum_{k=0}^{\infty} \frac{(a_1)_k \cdot (a_p)_k z^k}{(b_1)_k \cdot (b_q)_k k!} \quad (\text{A.1})$$

where $a_i, b_j, z \in \mathbb{C}$, with $i = 1, \dots, p$, $j = 1, \dots, q$ and $(a)_k$ is the Pochhammer symbol, i.e.,

$$(a)_0 = 1, \quad (\text{A.2})$$

$$(a)_k = a(a+1) \cdot (a+k-1), \quad k \geq 1. \quad (\text{A.3})$$

We underline that the hypergeometric function ${}_0F_1(; b; z)$ has only one parameter b in the denominator and no parameters a_i at the numerator.

References

- Achaoui, Y., Antonakakis, T., Br l , S., Craster, R.V., Enoch, S., Guenneau, S., 2017. Clamped seismic metamaterials: ultra-low frequency stop bands. *New J. Phys.* 19 (6), 063022.
- Achaoui, Y., Ungureanu, B., Enoch, S., Br l , S., Guenneau, S., 2016. Seismic waves damping with arrays of inertial resonators. *Extreme Mech. Lett.* 8, 30–37, Nanomechanics: Bridging Spatial and Temporal Scales.
- Airoldi, L., Ruzzene, M., 2011. Design of tunable acoustic metamaterials through periodic arrays of resonant shunted piezos. *New J. Phys.* 13 (11), 113010.
- Al-Ketan, O., Rowshan, R., Al-Rub, R.K.A., 2018. Topology-mechanical property relationship of 3D printed strut, skeletal, and sheet based periodic metallic cellular materials. *Addit. Manuf.* 19, 167–183.
- Alan, S., Allam, A., Erturk, A., 2019. Programmable mode conversion and bandgap formation for surface acoustic waves using piezoelectric metamaterials. *Appl. Phys. Lett.* 115 (9), 093502.
- Alshaqaq, M., Erturk, A., 2020. Graded multifunctional piezoelectric metastructures for wideband vibration attenuation and energy harvesting. *Smart Mater. Struct.* 30 (1), 015029.
- Antoulas, A.C., 2005. Approximation of Large-Scale Dynamical Systems. In: *Advances in Design and Control*, vol. 6, Society for Industrial and Applied Mathematics (SIAM), Philadelphia, PA, p. xxvi+479.
- Arena, A., Bacigalupo, A., Lepidi, M., 2022. Wave propagation in viscoelastic metamaterials via added-state formulation. *International Journal of Mechanical Sciences* 228, 107461.
- Bacigalupo, A., De Bellis, M.L., Gnecco, G., 2019. Complex frequency band structure of periodic thermo-diffusive materials by Floquet–Bloch theory. *Acta Mech.* 230 (9), 3339–3363.
- Bacigalupo, A., De Bellis, M.L., Misseroni, D., 2020. Design of tunable acoustic metamaterials with periodic piezoelectric microstructure. *Extreme Mech. Lett.* 40, 100977.
- Bacigalupo, A., De Bellis, M.L., Vasta, M., 2022. Design of tunable hierarchical waveguides based on Fibonacci-like microstructure. *Int. J. Mech. Sci.* 224, 107280.
- Bacigalupo, A., Gambarotta, L., 2016. Simplified modelling of chiral lattice materials with local resonators. *Int. J. Solids Struct.* 83, 126–141.
- Bacigalupo, A., Gambarotta, L., 2017. Wave propagation in non-centrosymmetric beam-lattices with lumped masses: discrete and micropolar modeling. *Int. J. Solids Struct.* 118, 128–145.
- Barchiesi, E., Spagnuolo, M., Placidi, L., 2019. Mechanical metamaterials: A state of the art. *Math. Mech. Solids* 24 (1), 212–234.
- Beli, D., Arruda, J., Ruzzene, M., 2018. Wave propagation in elastic metamaterial beams and plates with interconnected resonators. *Int. J. Solids Struct.* 139–140, 105–120.
- Bergamini, A.E., Z ndel, M., Flores Parra, E.A., Delpero, T., Ruzzene, M., Ermanni, P., 2015. Hybrid dispersive media with controllable wave propagation: A new take on smart materials. *J. Appl. Phys.* 118 (15), 154310.
- Berrut, J.-P., De Marchi, S., Elefante, G., Marchetti, F., 2020. Treating the Gibbs phenomenon in barycentric rational interpolation and approximation via the S-Gibbs algorithm. *Appl. Math. Lett.* 103, 106196, 7.
- Bhatt, A., Banerjee, A., 2022. Double attenuation peaks in metamaterial with simultaneous negative mass and stiffness. *Phys. Lett. A* 128201.
- Bordiga, G., Cabras, L., Piccolroaz, A., Bigoni, D., 2021. Dynamics of prestressed elastic lattices: homogenization, instabilities, and strain localization. *Journal of the Mechanics and Physics of Solids* 146, 104198.
- Bordiga, G., Piccolroaz, A., Bigoni, D., 2022. A way to hypo-elastic artificial materials without a strain potential and displaying flutter instability. *Journal of the Mechanics and Physics of Solids* 158, 104665.
- Br l , S., Javelaud, E., Enoch, S., Guenneau, S., 2014. Experiments on seismic metamaterials: Molding surface waves. *Phys. Rev. Lett.* 112, 133901.
- Brun, M., Guenneau, S., Movchan, A.B., 2009. Achieving control of in-plane elastic waves. *Appl. Phys. Lett.* 94, 061903.
- Brun, B., Moreau, N., Somanchi, S., Nguyen, V.H., Watanabe, K., Taniguchi, T., Charlier, J., Stampfer, C., Hackens, B., 2019. Imaging Dirac fermions flow through a circular veselago lens. *Phys. Rev. B* 100, 041401(R).
- Cabras, L., Brun, M., 2016. A class of auxetic three-dimensional lattices. *J. Mech. Phys. Solids* 91, 56–72.
- Carta, G., Movchan, A.B., Argani, L.P., Bursi, O.S., 2016. Quasi-periodicity and multi-scale resonators for the reduction of seismic vibrations in fluid-solid systems. *Internat. J. Engrg. Sci.* 109, 216–239.
- Casadei, F., Ruzzene, M., Dozio, L., Cunefare, K., 2009. Broadband vibration control through periodic arrays of resonant shunts: experimental investigation on plates. *Smart Mater. Struct.* 19 (1), 015002.
- Celli, P., Gonella, S., Tajeddini, V., Muliana, A., Ahmed, S., Ounaies, Z., 2017. Wave control through soft microstructural curling: bandgap shifting, reconfigurable anisotropy and switchable chirality. *Smart Mater. Struct.* 26 (3), 035001.
- Celli, P., Zhang, W., Gonella, S., 2018. Pathway towards programmable wave anisotropy in cellular metamaterials. *Phys. Rev. Appl.* 9, 014014.
- Chen, S., Fan, Y., Fu, Q., Wu, H., Jin, Y., Zheng, J., Zhang, F., 2018. A review of tunable acoustic metamaterials. *Appl. Sci.* 8 (9), 1480.
- Chen, Y., Hu, G., Huang, G., 2017. A hybrid elastic metamaterial with negative mass density and tunable bending stiffness. *J. Mech. Phys. Solids* 105, 179–198.
- Chen, X., Moughames, J., Ji, Q., Mart nez, J.A.I., Tan, H., Ulliac, G., Laude, V., Kadic, M., 2022. 3D lightweight mechanical metamaterial with nearly isotropic inelastic large deformation response. *J. Mech. Phys. Solids* 105057.
- Collet, M., Ouisse, M., Ichchou, M.N., 2012. Structural energy flow optimization through adaptive shunted piezoelectric metacomposites. *J. Intell. Mater. Syst. Struct.* 23 (15), 1661–1677.
- Colombi, A., Colquitt, D., Roux, P., Guenneau, S., Craster, R.V., 2016. A seismic metamaterial: The resonant metawedge. *Sci. Rep.* 6, 27717.
- Colquitt, D., Brun, M., Gei, M., Movchan, A., Movchan, N., Jones, I., 2014. Transformation elastodynamics and cloaking for flexural waves. *J. Mech. Phys. Solids* 72, 131–143.
- Cummer, S.A., Christensen, J., Al , A., 2016. Controlling sound with acoustic metamaterials. *Nat. Rev. Mater.* 1.3, 16001.
- De Bellis, M.L., Bacigalupo, A., Zavarise, G., 2019. Characterization of hybrid piezoelectric nanogenerators through asymptotic homogenization. *Comput. Methods Appl. Mech. Engrg.* 355, 1148–1186.
- De Marchi, S., Elefante, G., Marchetti, F., 2021. Stable discontinuous mapped bases: the gibbs-runge-avoiding stable polynomial approximation (GRASPA) method. *J. Comput. Appl. Math.* 40 (8), Paper No. 299, 17.
- De Ponti, J.M., Colombi, A., Riva, E., Ardito, R., Braghin, F., Corigliano, A., Craster, R.V., 2020. Experimental investigation of amplification, via a mechanical delay-line, in a rainbow-based metamaterial for energy harvesting. *Appl. Phys. Lett.* 117 (14), 143902.
- dell'Isola, F., Maurini, C., Porfiri, M., 2004. Passive damping of beam vibrations through distributed electric networks and piezoelectric transducers: prototype design and experimental validation. *Smart Mater. Struct.* 13 (2), 299.
- Diana, V., Bacigalupo, A., Gambarotta, L., 2023. Thermodynamically-consistent dynamic continualization of block-lattice materials. *Int. J. Solids Struct.* 262, 112050.
- Dwivedi, A., Banerjee, A., Bhattacharya, B., 2020. Simultaneous energy harvesting and vibration attenuation in piezo-embedded negative stiffness metamaterial. *J. Intell. Mater. Syst. Struct.* 31 (8), 1076–1090.
- Fantoni, F., Bacigalupo, A., Gnecco, G., Gambarotta, L., 2023. Multi-objective optimal design of mechanical metafilters based on principal component analysis. *Int. J. Mech. Sci.* 248, 108195.

- Flores Parra, E.A., Bergamini, A., Lossouarn, B., Van Damme, B., Cenedese, M., Ermanni, P., 2017. Bandgap control with local and interconnected LC piezoelectric shunts. *Appl. Phys. Lett.* 111 (11), 111902.
- Forward, R.L., 1979. Electronic damping of vibrations in optical structures. *Appl. Opt.* 18, 690–697.
- Gavazzoni, M., Foletti, S., Pasini, D., 2022. Cyclic response of 3D printed metamaterials with soft cellular architecture: the interplay between as-built defects, material and geometric non-linearity. *J. Mech. Phys. Solids* 158, 104688.
- Ghaffarivardavagh, R., Nikolajczyk, J., Glynn Holt, R., Anderson, S., Zhang, X., 2018. Horn-like space-coiling metamaterials toward simultaneous phase and amplitude modulation. *Nature Commun.* 9 (1), 1–8.
- Gottlieb, D., Shu, C.-W., 1997. On the Gibbs phenomenon and its resolution. *SIAM Rev.* 39 (4), 644–668.
- Guo, J., Ye, C., Liu, C., Zhang, M., Li, C., Li, J., Shi, Y., Dai, D., 2020. Ultra-compact and ultra-broadband guided-mode exchangers on silicon. *Laser Photonics Rev.* 14 (7), 2000058.
- Hagood, N.W., von Flotow, A., 1991. Damping of structural vibrations with piezoelectric materials and passive electrical networks. *J. Sound Vib.* 146 (2), 243–268.
- Hollkamp, J.J., 1994. Multimodal passive vibration suppression with piezoelectric materials and resonant shunts. *J. Intell. Mater. Syst. Struct.* 5 (1), 49–57.
- Hou, Z., Assouar, B., 2018. Tunable elastic parity-time symmetric structure based on the shunted piezoelectric materials. *J. Appl. Phys.* 123 (8), 085101.
- Hu, G., Tang, L., Liang, J., Lan, C., Das, R., 2021. Acoustic-elastic metamaterials and phononic crystals for energy harvesting: A review. *Smart Mater. Struct.* 30 (8), 085025.
- Iannace, G., Ciaburro, G., Trematerra, A., 2021. Metamaterials acoustic barrier. *Appl. Acoust.* 181, 108172.
- Iyer, S., Venkatesh, T., 2014. Electromechanical response of (3–0,3–1) particulate, fibrous, and porous piezoelectric composites with anisotropic constituents: A model based on the homogenization method. *Int. J. Solids Struct.* 51 (6), 1221–1234.
- Jerri, A.J., 1998. *The Gibbs Phenomenon in Fourier Analysis, Splines and Wavelet Approximations*, Vol. 446. Springer Science & Business Media.
- Ji, G., Huber, J., 2022. Recent progress in acoustic metamaterials and active piezoelectric acoustic metamaterials - A review. *Appl. Mater. Today* 26, 101260.
- Jia, Z., Wang, L., 2019. 3D printing of biomimetic composites with improved fracture toughness. *Acta Mater.* 173, 61–73.
- Jian, Y., Tang, L., Hu, G., Li, Z., Aw, K.C., 2022. Design of graded piezoelectric metamaterial beam with spatial variation of electrodes. *Int. J. Mech. Sci.* 218, 107068.
- Kumar, P., Ali, T., Pai, M.M., 2021. Electromagnetic metamaterials: A new paradigm of antenna design. *IEEE Access* 9, 18722–18751.
- Lee, H.J., Zhang, S., Bar-Cohen, Y., Sherrit, S., 2014. High temperature, high power piezoelectric composite transducers. *Sensors* 14 (8), 14526–14552.
- Liao, Y.-L., Zhao, Y., 2020. Ultra-narrowband dielectric metamaterial absorber with ultra-sparse nanowire grids for sensing applications. *Sci. Rep.* 10 (1), 1–7.
- Lietaert, P., Meerbergen, K., Pérez, J., Vandereycken, B., 2022. Automatic rational approximation and linearization of nonlinear eigenvalue problems. *IMA J. Numer. Anal.* 42 (2), 1087–1115.
- Lu, Z., Wang, Q., Li, X., Yang, Z., 2017. Elastic properties of two novel auxetic 3D cellular structures. *Int. J. Solids Struct.* 124, 46–56.
- Mackey, D.S., Mackey, N., Mehl, C., Mehrmann, V., 2006a. Structured polynomial eigenvalue problems: good vibrations from good linearizations. *SIAM J. Matrix Anal. Appl.* 28 (4), 1029–1051.
- Mackey, D.S., Mackey, N., Mehl, C., Mehrmann, V., 2006b. Vector spaces of linearizations for matrix polynomials. *SIAM J. Matrix Anal. Appl.* 28 (4), 971–1004.
- Marakakis, K., Tairidis, G.K., Koutsianitis, P., Stavroulakis, G.E., 2019. Shunt piezoelectric systems for noise and vibration control: A review. *Front. Built Environ.* 5, 64.
- Mathai, A.M., Saxena, R.K., 2006. *Generalized Hypergeometric Functions with Applications in Statistics and Physical Sciences*, Vol. 348. Springer.
- Mehrmann, V., Voss, H., 2004. Nonlinear eigenvalue problems: A challenge for modern eigenvalue methods. *GAMM Mitt. Ges. Angew. Math. Mech.* 27 (2), 121–152 (2005).
- Miniaci, M., Krushynska, A., Pugno, F.B.N., 2016. Large scale mechanical metamaterials as seismic shields. *New J. Phys.* 18, 083041.
- Misseroni, D., Colquitt, D., Movchan, A., Movchan, N., Jones, I., 2016. Cymatics for the cloaking of flexural vibrations in a structured plate. *Sci. Rep.* 6, 23929.
- Momeni, K., Mofidian, S.M., Bardaweel, H., 2019. Systematic design of high-strength multicomponent metamaterials. *Mater. Des.* 183, 108124.
- Montgomery, S.M., Kuang, X., Armstrong, C.D., Qi, H.J., 2020. Recent advances in additive manufacturing of active mechanical metamaterials. *Curr. Opin. Solid State Mater. Sci.* 24 (5), 100869.
- Mu, D., Shu, H., Zhao, L., An, S., 2020. A review of research on seismic metamaterials. *Adv. Eng. Mater.* 22 (4), 1901148.
- Norris, A.N., Shuvalov, A.L., 2011. Elastic cloaking theory. *Wave Motion* 48, 525–538.
- Ouisse, M., Collet, M., Scarpa, F., 2016. A piezo-shunted kirigami auxetic lattice for adaptive elastic wave filtering. *Smart Mater. Struct.* 25 (11), 115016.
- Park, J., Park, C., Lee, K., Lee, S., 2015. Acoustic superlens using membrane-based metamaterials. *Appl. Phys. Lett.* 106 (5), 051901.
- Pishvar, M., Harne, R.L., 2020. Foundations for soft, smart matter by active mechanical metamaterials. *Adv. Sci.* 7 (18), 2001384.
- Preumont, A., 1997. *Vibration Control of Active Structures*, Vol. 2. Springer.
- Ruhe, A., 1973. Algorithms for the nonlinear eigenvalue problem. *SIAM J. Numer. Anal.* 10, 674–689.
- Sangiorgio, V., Parisi, F., Fieni, F., Parisi, N., 2022. The new boundaries of 3D-printed clay bricks design: Printability of complex internal geometries. *Sustainability* 14 (2).
- Shizgal, B.D., Jung, J.-H., 2003. Towards the resolution of the Gibbs phenomena. *J. Comput. Appl. Math.* 161 (1), 41–65.
- Stenger, N., Wilhelm, M., Wegener, M., 2012. Experiments on elastic cloaking in thin plates. *Phys. Rev. Lett.* 108 (1), 014301.
- Su, Y., Bai, Z., 2011. Solving rational eigenvalue problems via linearization. *SIAM J. Matrix Anal. Appl.* 32 (1), 201–216.
- Tadesse, A.D., Acharya, O.P., Sahu, S., 2020. Application of metamaterials for performance enhancement of planar antennas: a review. *Int. J. RF Microw. Comput.-Aided Eng.* 30 (5), e22154.
- Thomas, O., Deü, J., Ducarne, J., 2009. Vibrations of an elastic structure with shunted piezoelectric patches: efficient finite element formulation an electromechanical coupling coefficients. *Internat. J. Numer. Methods Engrg.* 80, 235–268.
- Thorp, O., Ruzzene, M., Baz, A., 2001. Attenuation and localization of wave propagation in rods with periodic shunted piezoelectric patches. *Smart Mater. Struct.* 10 (5), 979.
- Vadalá, F., Bacigalupo, A., Lepidi, M., Gambarotta, L., 2021. Free and forced wave propagation in beam lattice metamaterials with viscoelastic resonators. *Int. J. Mech. Sci.* 193, 106129.
- Wang, Y., Guo, J., Fang, Y., Zhang, X., Yu, H., 2021. Ultralight metamaterial for sound absorption based on miura-ori tessellation structures. *Adv. Eng. Mater.* 23 (12), 2100563.
- Wang, G., Wang, J., Chen, S., Wen, J., 2011. Vibration attenuations induced by periodic arrays of piezoelectric patches connected by enhanced resonant shunting circuits. *Smart Mater. Struct.* 20 (12), 125019.
- Willey, C., Buskohl, P., Juhl, A., 2020. Electronically tunable auxetic behavior of shunted piezoelectric elements. *J. Mech. Phys. Solids* 137, 103873.
- Xiang, L., Wang, G., Zhu, C., 2022. Controlling sound transmission by space-coiling fractal acoustic metamaterials with broadband on the subwavelength scale. *Appl. Acoust.* 188, 108585.
- Xiao, S., Wang, T., Liu, T., Zhou, C., Jiang, X., Zhang, J., 2020. Active metamaterials and metadevices: a review. *J. Phys. D: Appl. Phys.* 53 (50), 503002.
- Yan, X., Zhu, R., Huang, G., Yuan, F.G., 2013. Focusing guided waves using surface bonded elastic metamaterials. *Appl. Phys. Lett.* 103 (12), 121901.
- Yi, K., Collet, M., 2021. Broadening low-frequency bandgaps in locally resonant piezoelectric metamaterials by negative capacitance. *J. Sound Vib.* 493, 115837.
- Yin, S., Guo, W., Wang, H., Huang, Y., Yang, R., Hu, Z., Chen, D., Xu, J., Ritchie, R.O., 2021. Strong and tough bioinspired additive-manufactured dual-phase mechanical metamaterial composites. *J. Mech. Phys. Solids* 149, 104341.
- Yuan, S., Chua, C.K., Zhou, K., 2019. 3D-printed mechanical metamaterials with high energy absorption. *Adv. Mater. Technol.* 4 (3), 1800419.
- Zangeneh-Nejad, F., Fleury, R., 2019. Active times for acoustic metamaterials. *Rev. Phys.* 4, 100031.
- Zhang, H., Chen, Y., Liu, X., Hu, G., 2020. An asymmetric elastic metamaterial model for elastic wave cloaking. *J. Mech. Phys. Solids* 135, 103796.
- Zhang, H., Wen, J., Xiao, Y., Wang, G., Wen, X., 2015. Sound transmission loss of metamaterial thin plates with periodic subwavelength arrays of shunted piezoelectric patches. *J. Sound Vib.* 343, 104–120.
- Zhang, W., Xu, J., 2022. Ultra-light kirigami lantern chain for superior impact mitigation. *Extreme Mech. Lett.* 51, 101602.
- Zhang, Z., Zhang, L., Song, B., Yao, Y., Shi, Y., 2022. Bamboo-inspired, simulation-guided design and 3D printing of light-weight and high-strength mechanical metamaterials. *Appl. Mater. Today* 26, 101268.